

Transmission Electron Microscopy Analysis of Corroded Metal Waste Forms

prepared by
Chemical Engineering Division
Argonne National Laboratory

About Argonne National Laboratory

Argonne is managed by The University of Chicago for the U.S. Department of Energy under contract W-31-109-Eng-38. The Laboratory's main facility is outside Chicago, at 9700 South Cass Avenue, Argonne, Illinois 60439. For information about Argonne and its pioneering science and technology programs, see www.anl.gov.

Availability of This Report

This report is available, at no cost, at <http://www.osti.gov/bridge>. It is also available on paper to U.S. Department of Energy and its contractors, for a processing fee, from:

U.S. Department of Energy
Office of Scientific and Technical Information
P.O. Box 62
Oak Ridge, TN 37831-0062
phone (865) 576-8401
fax (865) 576-5728
reports@adonis.osti.gov

Disclaimer

This report was prepared as an account of work sponsored by an agency of the United States Government. Neither the United States Government nor any agency thereof, nor The University of Chicago, nor any of their employees or officers, makes any warranty, express or implied, or assumes any legal liability or responsibility for the accuracy, completeness, or usefulness of any information, apparatus, product, or process disclosed, or represents that its use would not infringe privately owned rights. Reference herein to any specific commercial product, process, or service by trade name, trademark, manufacturer, or otherwise, does not necessarily constitute or imply its endorsement, recommendation, or favoring by the United States Government or any agency thereof. The views and opinions of document authors expressed herein do not necessarily state or reflect those of the United States Government or any agency thereof, Argonne National Laboratory, or The University of Chicago.

ANL-05/09

ARGONNE NATIONAL LABORATORY
9700 South Cass Avenue
Argonne, IL 60439-4837

**TRANSMISSION ELECTRON MICROSCOPY ANALYSIS OF
CORRODED EBR II METALLIC WASTE FORMS**

by

Nancy L. Dietz

Chemical Engineering Division

February 2005

ACRONYMS

AES	Auger Emission Spectroscopy
CDSP	Co-Disposal Packages
CRWMS	Civilian Radioactive Waste Management System
EBR-II	Experimental Breeder Reactor-II
ED	Electron Diffraction
EDS	Energy Dispersive X-Ray Emission Spectroscopy
HLW	High-Level Radioactive Waste
ICP-MS	Inductively Coupled Plasma-Mass Spectrometry
IM	Intermetallic Material
MCC-1	Material Characterization Center-Static Leach Test Number 1
MWF	Metallic Waste Form
NL(<i>i</i>)	Normalized Elemental Mass Loss (based on element <i>i</i>)
PCT	Product Consistency Test
SEM	Scanning Electron Microscope (or Microscopy)
STEM	Scanning Transmission Electron Microscopy
SS	Stainless Steel
S/V	Solid Surface Area-to-Solution Volume Ratio
TEM	Transmission Electron Microscope (or Microscopy)
VHT	Vapor Hydration Test

TABLE OF CONTENTS

	Page
ACRONYMS	ii
ABSTRACT	vii
1.0 INTRODUCTION	1
1.1 Background.....	1
1.2 Summary.....	2
2.0 MWF TEM ANALYSIS	3
2.1 316SS-15Zr-5U.....	4
2.1.1 Experimental: <i>Immersion Test, 90 °C for 14 days in 1000 ppm KCl</i>	4
2.1.2 Results.....	4
2.1.3 Discussion	13
2.1.4 Summary	15
2.2 304SS-40Zr Intermetallic	15
2.2.1 Experimental: <i>Vapor Hydration Test, 200 °C for 56 days</i>	15
2.2.2 Results.....	16
2.2.3 Discussion	19
2.2.4 Summary	21
2.3 316SS-15Zr.....	22
2.3.1 Experimental: <i>Vapor Hydration Test, 200 °C for 365 days</i>	22
2.3.2 Results and Discussion	22
2.3.3 Summary	24
2.4 316SS-15Zr-0.5Ag-1.5Pd-2Ru	25
2.4.1 Experimental: <i>Immersion Test, 200 °C for 91 days in deionized water</i> ...	25
2.4.2 Results and Discussion	26
2.4.3 Summary	28
2.5 316SS-15Zr-11U-0.1Pd-0.6Ru-0.3Tc and SS-15Zr-2U-1Nb-1Rh-Ru-1Tc	30
2.5.1 Experimental: <i>Immersion Tests, 90 °C for 400 and 700 days</i>	30
2.5.2 Results.....	30
2.5.3 Summary	33
2.6 316SS-15Zr-5U.....	34
2.6.1 Experimental: <i>Pulsed-Flow Immersion Test, 90 °C for >445 day</i>	34
2.6.2 Results and Discussion	34
2.6.3 Summary	34
3.0 LOCALIZED CORROSION	35
4.0 RECOMMENDATIONS FOR FUTURE WORK.....	37
ACKNOWLEDGEMENTS.....	39
REFERENCES	40

LIST OF FIGURES

	Page
1. Cross-section of corrosion layer from a region of the surface that appeared unreacted	5
2. Cross-section of corrosion layer showing darker agglomerates	6
3. Corrosion layer showing Pd grains over the corroded surface and the nano-crystalline agglomerate grains.....	6
4. Cross-section of corrosion layer from area of uniform thickness	7
5. Corrosion layer from heavily corroded region.....	8
6. Darkfield image of “interfacial” layer showing presence of small crystallites.....	9
7. Surface agglomerate showing dark “inclusions”	10
8. Agglomerate close to the oxide/metal interface showing dark “inclusions”	10
9. Metal/oxide interface showing base metal attachment.....	11
10. EDS spectrum from piece of base metal in Figure 9.....	12
11. EDS spectrum of agglomerate adjacent to base metal as seen in Figure 9.....	12
12. Surface layers from different locations on 304SS40Zr vapor hydration tested sample	17
13. STEM image showing line of point analysis and STEM linescan plot.....	18
14. Cross sections of vapor hydration tests sample showing surface corrosion products formed over the steel phase.....	23
15. Corrosion products formed on the MWF intermetallic phase.....	24
16. Corrosion products formed on the MWF steel phase from immersion tests at 200°C for 91 days	26
17. Corrosion products on the MWF intermetallic phase from immersion tests 200°C for 91 days.....	27
18. STEM linescan for base metal components and doped noble metals	29
19. Corrosion products formed over the intermetallic and steels phases of Sample 31.....	31

LIST OF FIGURES
(Contd.)

	Page
20 Corrosion products formed over the intermetallic and steel phases of Sample 61	32
21. Corrosion layer over the intermetallic phase	35
22. SEM image showing region of localized corrosion on the reacted MWF	36
23. High magnification SEM image of an area from the area shown in Figure 22 and higher magnification of boxed area in Figure A showing extensive dendritic and grain boundary or interphase boundary dissolution	36

LIST OF TABLES

	Page
1. EDS Results from STEM Linescan Analysis	19
2. Elemental Compositions Measured with STEM and AES	21
3. EDS Analysis of Corrosion Products and Underlying Steel.....	23
4. EDS Analysis of Alteration Layer.....	24
5. Normalized Mass Loss of Elements from 316SS-15ZR-0.5Ag-1.5Pd-2Ru in Immersion Test in Deionized Water at 200°C for 91 Days	26
6. EDS Analysis of Corrosion Products Over Steel Phase in	27
7. EDS Analysis of Corrosion Products Over Intermetallic Phase	28
8. Normalized Mass Loss of Elements in Samples 31 and 61	30
9. EDS Analysis of MWF Surface Corrosion Products over Intermetallic and Steel Phases in Sample 31	31
10. EDS Analysis of MWF Surface Corrosion Products over Intermetallic and Steel Phases in Sample 61	33
11. EDS Analysis of MWF Surface Corrosion Products over the Intermetallic Phase	35

ABSTRACT

This report documents the results of analyses with transmission electron microscopy (TEM) combined with energy dispersive X-ray spectroscopy (EDS) and selected area electron diffraction (ED) of samples of metallic waste form (MWF) materials that had been subjected to various corrosion tests. The objective of the TEM analyses was to characterize the composition and microstructure of surface alteration products which, when combined with other test results, can be used to determine the matrix corrosion mechanism. The examination of test samples generated over several years has resulted in refinements to the TEM sample preparation methods developed to preserve the orientation of surface alteration layers and the underlying base metal. The preservation of microstructural spatial relationships provides valuable insight for determining the matrix corrosion mechanism and for developing models to calculate radionuclide release in repository performance models. The TEM results presented in this report show that oxide layers are formed over the exposed steel and intermetallic phases of the MWF during corrosion in aqueous solutions and humid air at elevated temperatures. An amorphous non-stoichiometric ZrO_2 layer forms at the exposed surfaces of the intermetallic phases, and several non-stoichiometric Fe-O layers form over the steel phases in the MWF. These oxide layers adhere strongly to the underlying metal, and may be overlain by one or more crystalline Fe-O phases that probably precipitated from solution. The layer compositions are consistent with a corrosion mechanism of oxidative dissolution of the steel and intermetallic phases. The layers formed on the steel and intermetallic phases form a continuous layer over the exposed waste form, although vertical splits in the layer and corrosion in pits and crevices were seen in some samples. Additional tests and analyses are needed to verify that these layers passivate the underlying metals and if passivation can break down as the MWF corrodes. The importance of localized corrosion should also be determined.

1.0 INTRODUCTION

Argonne National Laboratory (ANL) has developed an electrometallurgical treatment process for sodium-bonded spent nuclear fuel from the Experimental Breeder Reactor-II [1]. This process stabilizes metallic sodium and separates uranium from fission products and transuranic elements that are contained in the fuel. The fission products and other waste constituents are immobilized in two waste forms: 1) a ceramic waste form that contains salt waste with transuranic elements, active fission products (Cs, Sr, I), and rare earth elements [2], and 2) a metal waste form (MWF) composed primarily of stainless steel wastes from cladding hulls and reactor hardware, and ~15 wt.% Zr, from the U-Zr and U-Pu-Zr alloy fuels [3-5]. The MWF contains noble metal fission products (Tc, Nb, Ru, Rh, Te, Ag, Pd, Mo) and small amounts of actinides. Both waste forms are intended for eventual disposal in the Yucca Mountain repository. Qualification of MWF materials for disposal will require an understanding of its chemical, physical, and radiological durability and a mechanistic understanding of matrix corrosion and radionuclide release. A model of the MWF degradation is being developed based on laboratory tests. The analyses summarized in this report can be used in both the development and validation of that model.

1.1. *Background*

The MWF has been subjected to a variety of leaching and corrosion tests to study its degradation and release of radionuclides. The purpose of testing is to evaluate long-term stability of the MWF under potential geologic repository conditions. These tests include: linear polarization, the product consistency test (PCT), immersion testing, the vapor hydration test (VHT), and air oxidation. Initial testing of the MWF was done with a 316SS-15Zr material to assess the corrosion behavior of the base metal composition. Later tests were conducted on 316SS-15Zr materials doped with individual fission product surrogates (Tc, Mo, Re, Ru, Rh, Pd, Nb, Ag) and actinides (U, Pu, Np). The purpose of tests with doped MWF has been to understand the fate of these elements during corrosion of the MWF. Subsequent transmission electron microscopy (TEM) analyses were performed on selected tested samples to determine microstructural and compositional changes that occurred as the MWF corroded under various test conditions. TEM analysis has the advantage of being able to detect these changes with high spatial and spectral resolution. In addition, topological information is provided at the microstructural level. This information facilitates interpretation of other test data that are important in understanding and modeling the mechanism of corrosion.

Corrosion testing has demonstrated that the MWF is very corrosion resistant under repository-relevant conditions. The stability of most reactive metals is due to the formation of an adherent protective surface oxide scale [6, 7]. Similarly, the durability of the MWF is attributed to protective oxide films that form over the steel and intermetallic phases. Studying these protective layers will help in understanding the behavior of the MWF during corrosion and the passivating role the layers probably serve. The layer(s) are typically too thin to be detected using other microscopic methods, such as optical microscopy or scanning electron microscopy (SEM), so TEM analysis is essential to resolve the intact oxide layer microstructure and obtain compositional and structural data.

This report includes TEM data obtained by analysis of MWF samples that were corroded in static and pulsed-flow immersion tests, and vapor hydration tests. The immersion tests were based on Materials Characterization Center test procedure number 1 (MCC-1). A monolith of the MWF was immersed in a static solution such as deionized water or simulated groundwater, at a specific temperature for a set time interval. The immersion tests in this report were conducted with a sample surface area to leachant volume (S/V) ratio of 50 m^{-1} . The solution elemental compositions were analyzed by inductively coupled plasma mass spectroscopy (ICP-MS) and the monoliths were examined for surface alteration. Optical microscopy, scanning electron microscopy, and transmission electron microscopy were used to study the formation of corrosion products. The pulsed-flow immersion test is similar to the static immersion test except that a portion of the test solution was sampled for analysis and replaced with fresh leachant periodically. This allows for studying element release as a function of time during the test. In the vapor hydration test, a monolith of the sample was exposed to water vapor at elevated temperature such that a thin static film of water remained on the sample surface throughout the test. This accelerates the corrosion process (relative to immersion tests) because of the higher temperature and higher sample surface area-to-solution volume (S/V) ratio that is attained. Saturation of the thin film of water in contact with the sample surface will result in precipitation and formation of alteration phases. Optical microscopy, scanning and transmission electron microscopy were used to study these alteration phases in order to gain a better understanding of MWF corrosion processes.

A considerable amount of method development occurred as each TEM analysis was conducted and with the preparation of each consecutive sample. Consequently, the increasing level and quality of data for succeeding samples reflects the improvement in sample preparation. The organization of this report reflects the evolution of sample preparation development. Thin sections were produced with a Leica Ultracut T Ultramicrotome and examined with a JEOL 2010 TEM.

1.2 *Summary*

Since 1997, several TEM analyses have been performed on the bulk (unreacted) MWF and on MWF samples corroded in various laboratory tests. The MWF has a eutectic microstructure consisting of an iron solid solution phase of ferrite and austenite and a ZrFe_2 -type Laves intermetallic phase. In the nominal MWF composition, the steel and intermetallic phases are present in a 1:1 volume ratio. Studies have identified different Laves polytypes in the ZrFe_2 intermetallic phase, and have established the predominant disposition of U in the cubic C15 polytype [8-10]. Layered and precipitated surface structures on the reacted MWF samples have been identified, but it is not known if or how these structures affect radionuclide release as the MWF corrodes.

Several TEM analyses have revealed a ZrO_2 layer that appears to form only over the intermetallic phase. This layer is thin, amorphous, and very adherent to the underlying base metal. Within this layer are nanocrystals containing Fe, Cr, and Ni [11]. On top of this layer are agglomerates of iron oxides. The development of a three-layer structure can be explained with the aid of previous oxidation studies of zircaloy alloys [12]. Included in these studies is the oxidation behavior of Zr(Fe/Cr)_2 intermetallic precipitates. The precipitates are present as the

same Laves phases that comprise the intermetallic structure in the MWF. Consequently, these studies have significance in understanding corrosion behavior in the MWF. During the initial stages of oxidation in zircaloy alloys, the oxidation of zirconium occurs first to form a thin layer of ZrO_2 . This occurs because the effective oxygen partial pressure for zirconium oxidation is lower than that required for oxidation of Fe, Cr, or Ni. At a later stage, an adherent iron oxide layer forms over the steel phase, and other iron oxide phases can overlay the surface oxides. It is likely that the outermost iron oxides precipitate from solution. The ZrO_2 layer and overlying iron oxides are commonly non-stoichiometric.

The importance of the structure to the passivating properties of a layer is currently uncertain, but some reports indicate that passivation breaks down as an initially amorphous layer crystallizes [13]. The crystallized state can be induced by such factors as electric fields (influenced by Cl^-), mechanical stresses or an increase in temperature [6]. A crystallized oxide layer is less protective than an amorphous layer because ion movement through the layer is facilitated by 3-dimensional defects, such as grain boundaries and dislocations. Uranium, which is present in the intermetallic phases, is released faster than other actinides and fission products, yet TEM observations using electron diffraction (ED) and high resolution TEM show the ZrO_2 layer over the intermetallic to be amorphous. We have not detected crystallization in this layer except in the form of small nanocrystals [11]. Preferential uranium release might not be associated with crystallization of this layer or with a breakdown of passivation. However, TEM analysis at only a few regions of the reacted MWF surface may not represent events in other areas where localized corrosion processes may occur, such as pitting and cracking. Those processes would be characterized by high local rates of dissolution. Consequently, dissolution rates can be very different across the surface and TEM analyses of localized areas may not correlate with overall corrosion behavior or the release of elements into solution.

Our observations of steel phase oxidation resemble the microstructures described in the limited number of TEM studies that characterized alteration layers on stainless steels. Most of these studies described a duplex oxide layer consisting of a fine-grained inner layer and a coarse-grained outer layer. The outer layer typically consisted of Fe_3O_4 , whereas the inner layer was a Cr-Ni spinel of non-stoichiometric composition. A mechanism for the growth of the double oxide layer is the formation of the inner layer by a solid-state growth process and the growth of the outer layer through precipitation of metal ions. The inner passive layer is usually described as being only a few nanometers thick, whereas the outer coarse-grained layer typically consists of large single crystals. In many regions of corroded MWF samples, Cr- and O-rich corrosion products were detected along the surface. This is consistent with the formation of Cr_2O_3 as a passivating layer in steels. However, only one study of a VHT sample generated energy dispersive spectroscopy (EDS) results suggesting the presence of a Cr-oxide phase, although iron oxides and hydroxides can serve in a passivating role under various aqueous conditions.

2.0 MWF TEM ANALYSIS

This section summarizes the results of TEM analyses performed on MWF samples of different compositions reacted under various test conditions. The composition of the MWF material and

the conditions under which the sample was reacted are summarized first, and then the TEM results are presented and discussed. The results of each analysis are summarized separately.

2.1 316SS-15Zr-5U

Several TEM analyses were performed on the corrosion products that formed on the surface of a 316SS-15wt. % Zr metal waste form sample doped with 5 wt. % depleted uranium (316SS-15Zr-5U) sample as part of an ongoing effort to understand MWF corrosion behavior. An understanding of corrosion behavior will help determine the long-term stability of the waste form in a geologic repository. Previous immersion and vapor hydration testing using deionized water resulted in negligible alteration of the MWF test samples as detected by SEM/EDS analysis. Consequently, a more aggressive immersion test was conducted using a chloride solution instead of water to produce a measurable amount of corrosion to allow for characterization of the reacted sample. After SEM analysis, a sample of the corrosion layer was thin-sectioned using an ultramicrotome for detailed microstructural analysis with the TEM. While TEM analysis does not examine the entire surface, the greater resolution in imaging and analysis makes it possible to detect and perform compositional analysis on an alteration layer from surfaces that may appear unreacted in the SEM.

2.1.1 *Experimental: Immersion Test, 90 °C for 14 days in 1000 ppm KCl*

The specimen was mounted in epoxy and then ground and polished to a 1200 grit final finish. This was done to expose a single planar surface to the corroding solution. The mounted sample was then subjected to a 14 day pulse flow immersion test in a Teflon vessel containing deionized water with 1000 ppm KCl at 90°C. After 14 days, the sample was removed from the vessel, air dried, and given a conductive coating of palladium to dissipate charge build-up in the SEM. After SEM analysis, TEM samples were prepared by coating the mounted sample with low-viscosity epoxy and then carefully extracting the entire polymerized epoxy coating containing the corrosion product layer off of the unreacted bulk metal. Using optical microscopy, small selected areas along the corrosion layer were sliced out of the epoxy extraction and then embedded in fresh epoxy. The embedded samples were oriented so that the alteration layer would be cross-sectioned in the ultramicrotome. The following surface features were embedded: a) the thickest corrosion product from a crevice at the ingot/epoxy interface, b) the general corrosion product found along most of the surface, and c) the surface of what appeared to be unreacted metal. Sections ranged from 50-100 nm thick and were collected onto an electron transparent (~20 nm) carbon substrate supported by a copper slotted grid. The sections were analyzed using brightfield imaging augmented by EDS for compositional analysis and electron diffraction (ED) for phase identification.

2.1.2 *Results*

The cross-sections from the various corroded regions along the surface show the complete alteration layer from the metal/layer interface to the Pd-coated surface. The layer consists of very small-grained agglomerates loosely bound in a porous microstructure. The alteration layers vary in thickness and, in the case of the thickest corrosion product, the size and distribution of the agglomerates. The EDS analyses of several agglomerates give a layer composition

consisting of Fe, O, Si, Cl, Ca, Al, P, Cr, Mn, and Ni—listed in approximate order of abundance. The amounts of Si and O detected in the layer were affected by contaminated carbon substrates that contained Si, O, and trace amounts of P. The contamination occurred during their manufacture and was caused by using the same evaporator to make SiO substrates. In addition, the epoxy contains Si, O, and trace amounts of Cl.

Figure 1 shows a cross-section of the corrosion product layer removed from a region of the surface that did not appear corroded during optical and SEM analysis. The layer thickness varied from approximately 0.3 to 1.5 μm over the sample and consists of a porous network of fine-grained agglomerates. The network along the surface that was in contact with the solution (labeled “Surface” in Figure 1) appears more densely packed than at the interface with the underlying MWF (labeled “Interface” in Figure 1). The dark thin surface layer is produced by the strongly diffracting layer of Pd that was deposited on the surface to dissipate charge buildup during previous SEM analysis.

Figure 2 shows an area of the layer that contains darker and larger agglomerates along the surface. This region might correspond to small orange clumps that were seen optically on the surface that otherwise looked unreacted. These darker surface agglomerates consist primarily of Fe and O. They differ from the average layer composition by the lack of Ca and Cr and are seen primarily at the thinner parts ($<0.5\ \mu\text{m}$) of the corrosion layer. An interesting aspect of these dark agglomerates is that there are large voids beneath them.

Figure 3 is a high magnification view at the surface showing some of the Pd grains that nucleated on the surface and the nanocrystalline nature of the underlying grains of agglomerated oxides. In some regions, the individual grains appear to be less than 20\AA in diameter.

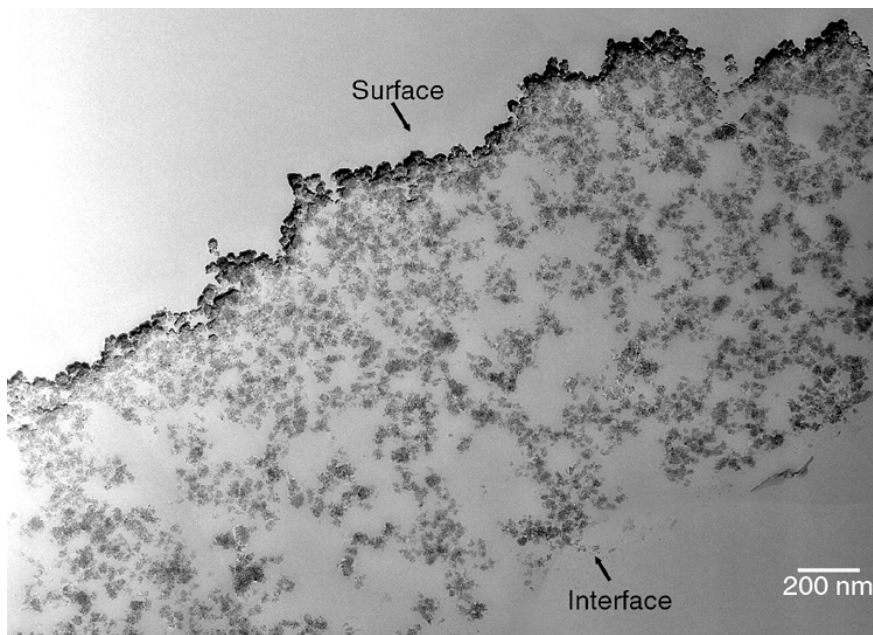


Figure 1. Cross-section of corrosion layer from a region of the surface that appeared unreacted.

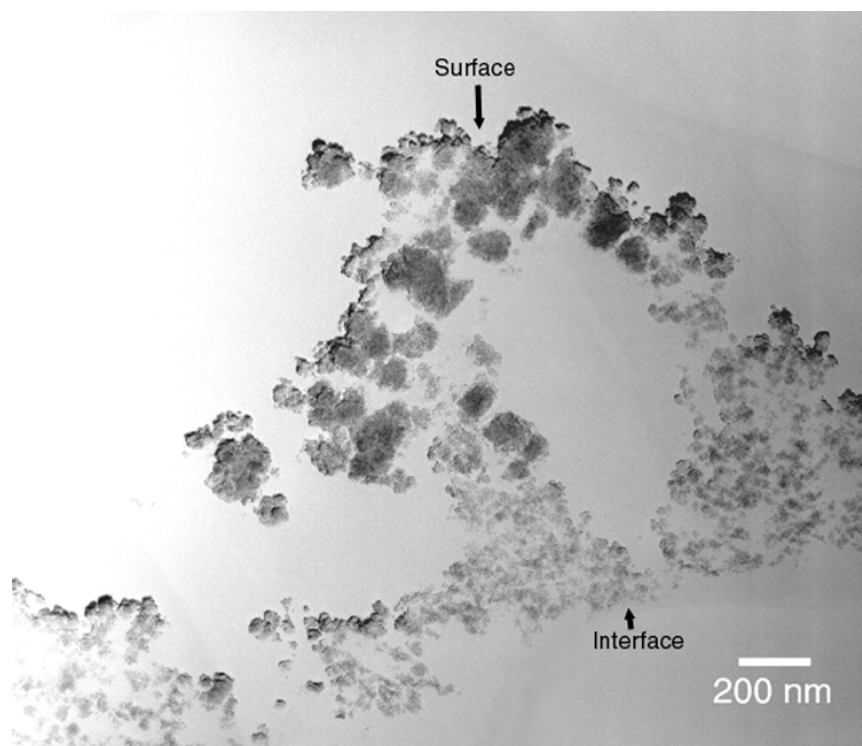


Figure 2. Cross-section of corrosion layer showing darker agglomerates.

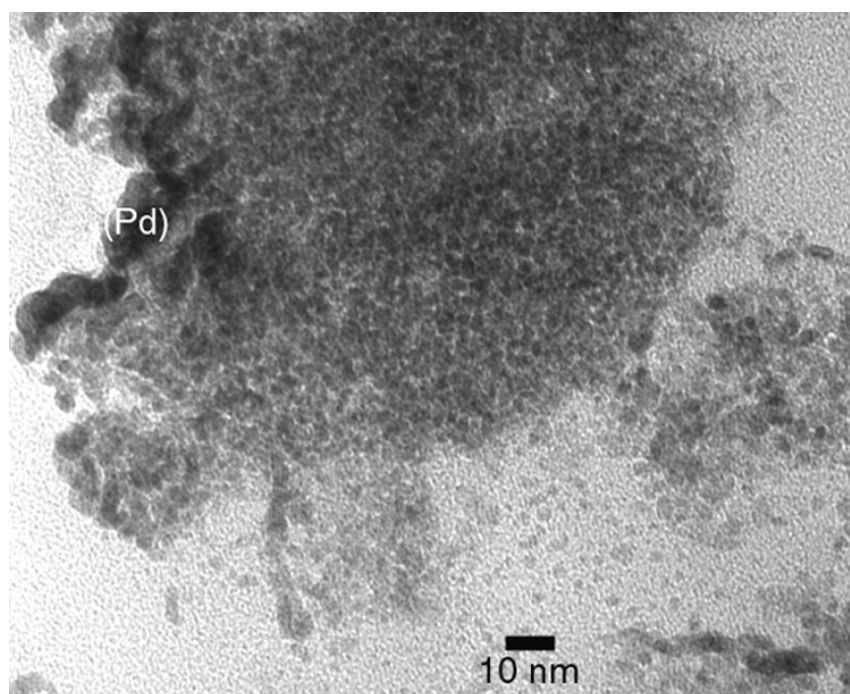


Figure 3. Corrosion layer showing Pd grains over the corroded surface and the nanocrystalline agglomerate grains.

Figure 4 shows the corrosion layer taken from relatively uniform region of the corrosion layer. Optically, this layer appears to be of uniform thickness and has an opaque orange color. The layer measures approximately $3.5\ \mu\text{m}$ thick. Besides being thicker and having a more uniform thickness than the “unreacted” appearing surface seen in Figure 1, the microstructure in Figure 4 is basically the same as that in Figure 1.

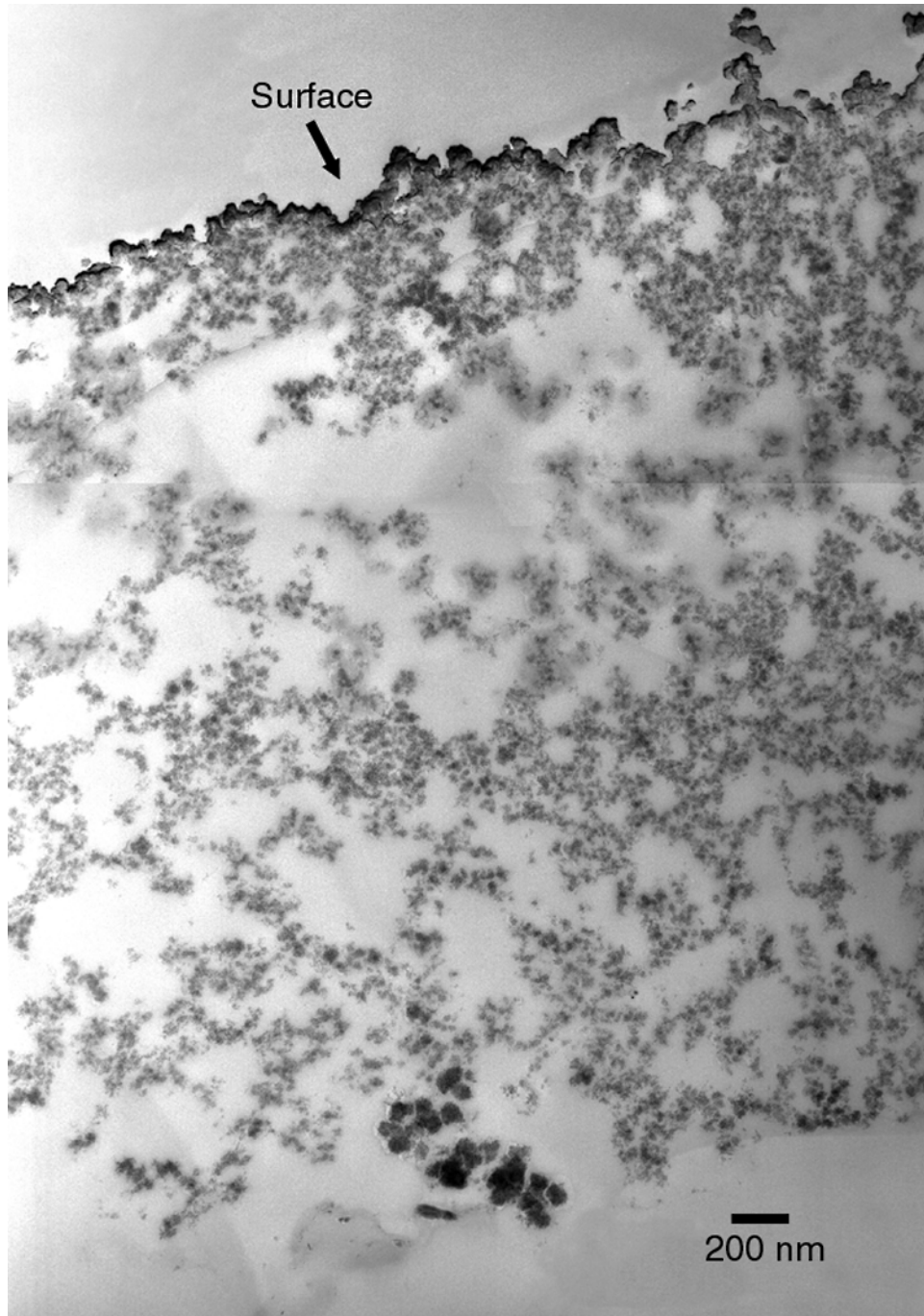


Figure 4. Cross-section of corrosion layer from area of uniform thickness.

The thickest corrosion product came from the crevice at the interface of the ingot and the mounting medium. This dark brown corrosion product was also present as isolated islands over pores on the ingot surface. Figure 5 shows a cross-section of this layer, which measures approximately 7.5 μm thick. The layer does not have a uniform thickness and increases to over 10 μm thick. The distinguishing features of this layer are: 1) a thin continuous layer at the metal/oxide interface, 2) an increasing size distribution of the agglomerates away from the interface, and 3) the presence of dark “inclusions” within many of the agglomerates. It should be

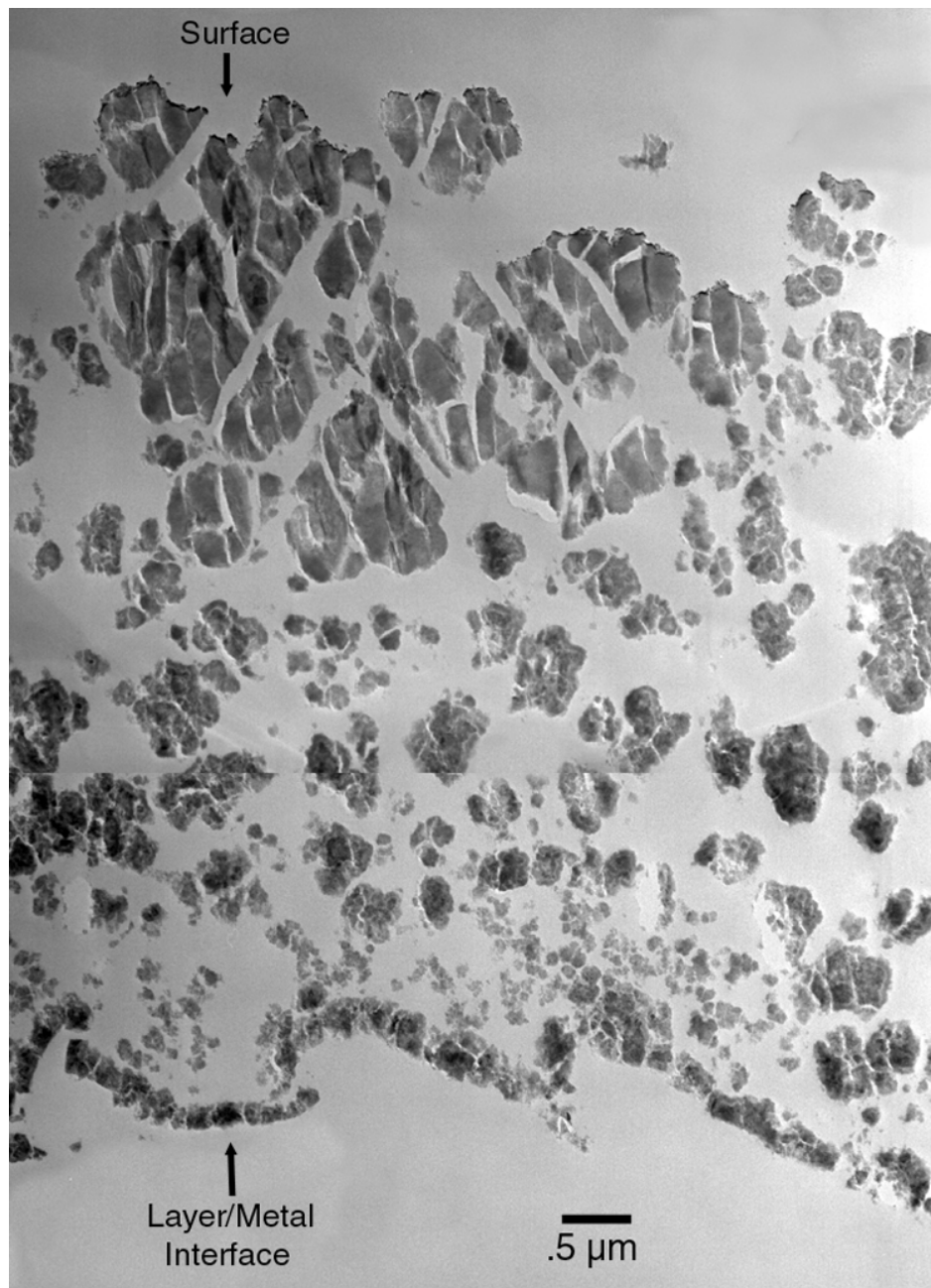


Figure 5. Corrosion layer from heavily corroded region.

noted that the gaps seen within the large agglomerates in Figure 5 are sectioning artifacts produced when the diamond knife struck a large area of dissimilar material. The interfacial region is approximately $0.4\ \mu\text{m}$ thick and consists of very fine grains.

Figure 6 is a darkfield image of the interfacial layer showing numerous small bright crystallites oriented at the Bragg angle from the optic axis. The layer composition was similar to the rest of the corrosion products. Above the thin interfacial layer, the agglomerates start to increase in size with distance away from the interface. The “middle” of the layer has an average agglomerate size of approximately $0.5\ \mu\text{m}$, while the agglomerates at the surface range from approximately 1 to $1.5\ \mu\text{m}$ in diameter. The “middle” layer agglomerate size appears uniform.

Many of the agglomerates contain dark “inclusions” consisting of nanocrystalline grains that are similar in size to the surrounding agglomerate grain size. Figures 7 and 8 show inclusions in agglomerates that are close to the surface (Figure 7) and to the metal/layer interface (Figure 8). The average size of the inclusions is 5 nm and does not seem to vary by location within the layer. Common to all the “inclusions” is the presence of Cr, Ni, and possibly Mn in addition to the elements listed above for the average agglomerate composition. The difficulty in detecting small amounts of Mn is due to overlap of the Cr $K_{\beta 1}$ line (5.947 keV) and the Mn $K_{\alpha 1}$ line (5.888 keV). There was no observable trend in the distribution of Ca and Cl. Both elements were detected in some inclusions and within some of the agglomerates throughout the alteration layer. Cr was always detected in the inclusions, but not always present in the agglomerate composition.

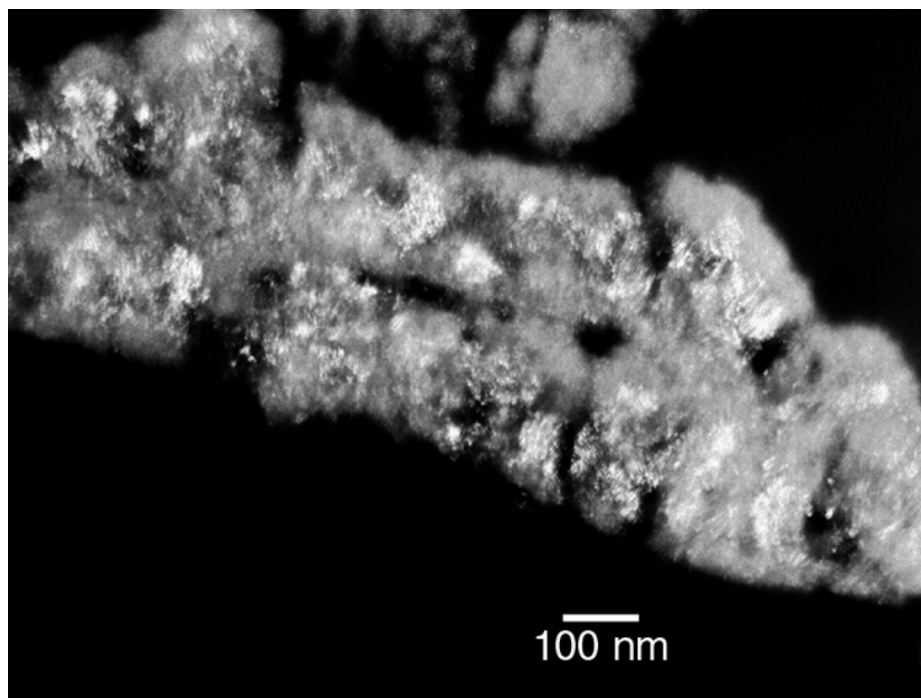


Figure 6. Darkfield image of “interfacial” layer showing presence of small crystallites (bright spots on image).

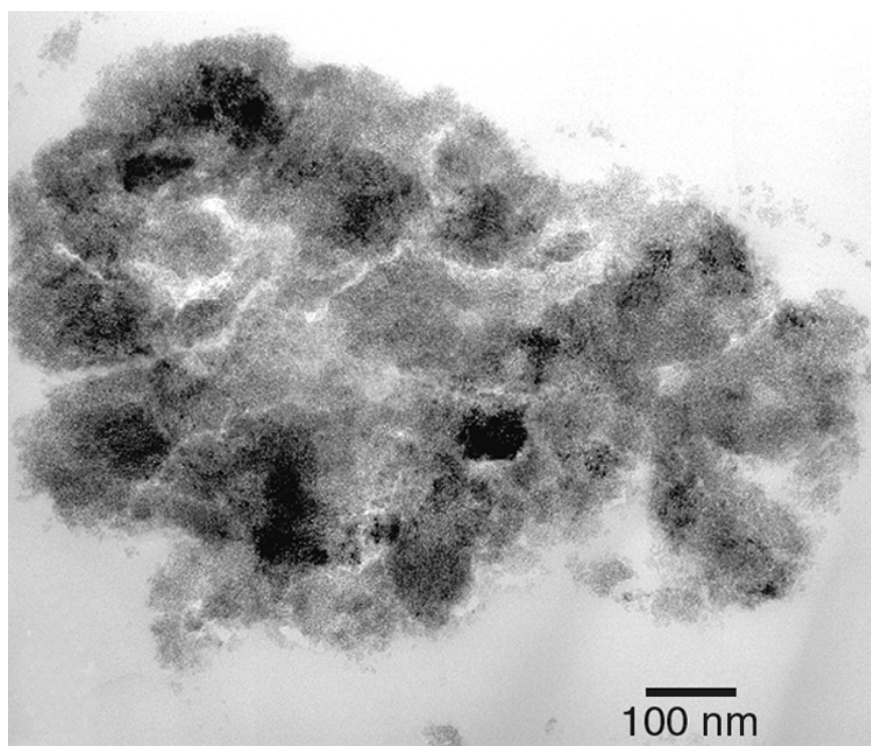


Figure 7. Surface agglomerate showing dark “inclusions”.

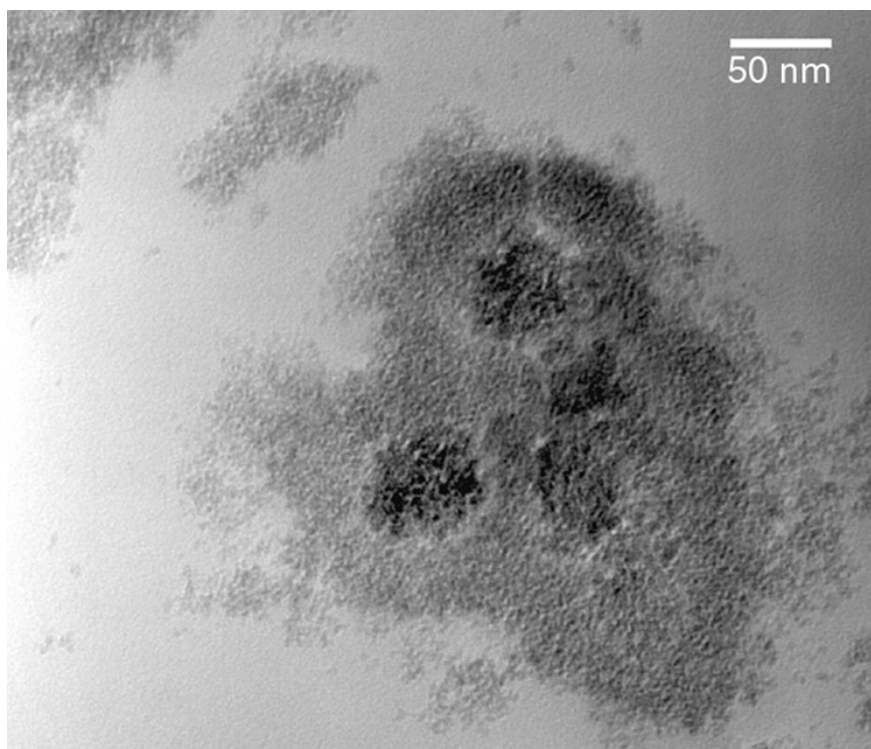


Figure 8. Agglomerate close to the oxide/metal interface showing dark “inclusions”.

Diffraction patterns taken from various regions throughout the layer show evidence of crystallinity. The patterns consisted of small spots that made up a ring. Because the entire layer is infiltrated with an amorphous embedding resin and the small size of the agglomerates, thicker sections were produced (~100 nm) so that more material would be available for electron diffraction. However, the diffraction patterns obtained from the thicker sections did not appear to show any more crystallinity than the thin sections, even when using the largest selected area diffraction aperture. Electron diffraction results indicate that hematite (Fe_2O_3) is present in the large surface agglomerates. It is difficult to determine if any part of the corrosion product is amorphous because of the large contribution of the amorphous epoxy and the underlying amorphous substrate to the diffraction pattern. However, it would not be entirely unexpected, because amorphous corrosion products in steels have been reported in the literature.

The extraction technique used to remove the alteration layer was successful in pulling off the entire corrosion layer and, on occasion, some of the underlying metal. Figure 9 shows a piece of base metal still attached to the alteration layer. The EDS spectra from the base metal and the agglomerate near the metal/layer interface are given in Figures 10 and 11, respectively. Notice that small amounts of Zr and U are present in the base metal but not in the agglomerate.

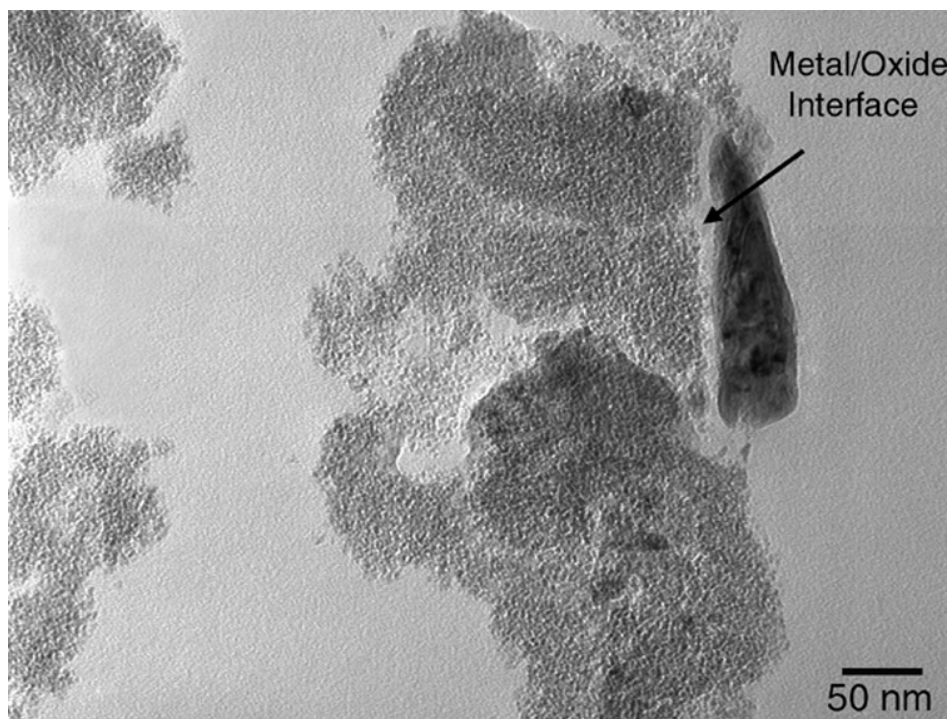


Figure 9. Metal/oxide interface showing base metal attachment.

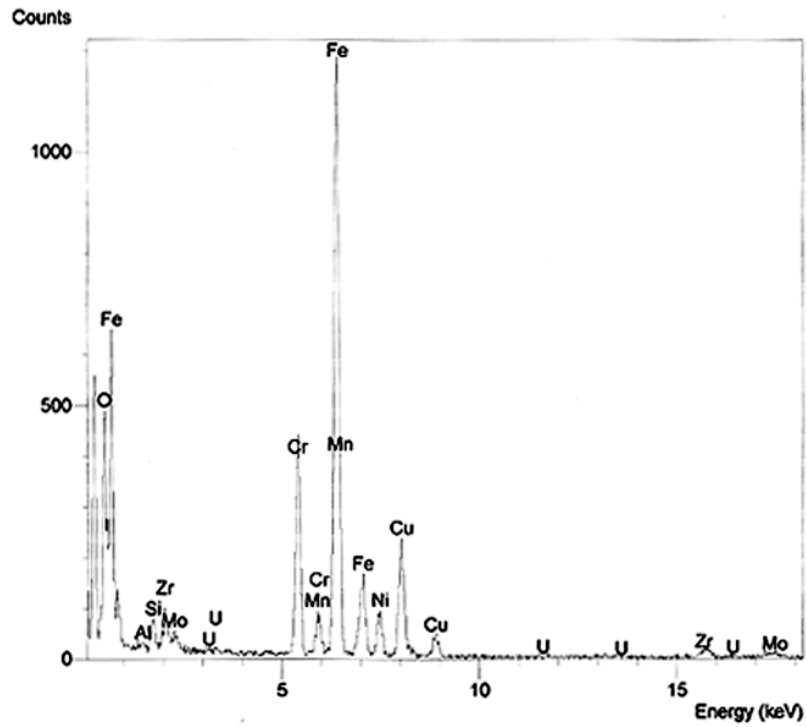


Figure 10. EDS spectrum from piece of base metal in Figure 9.

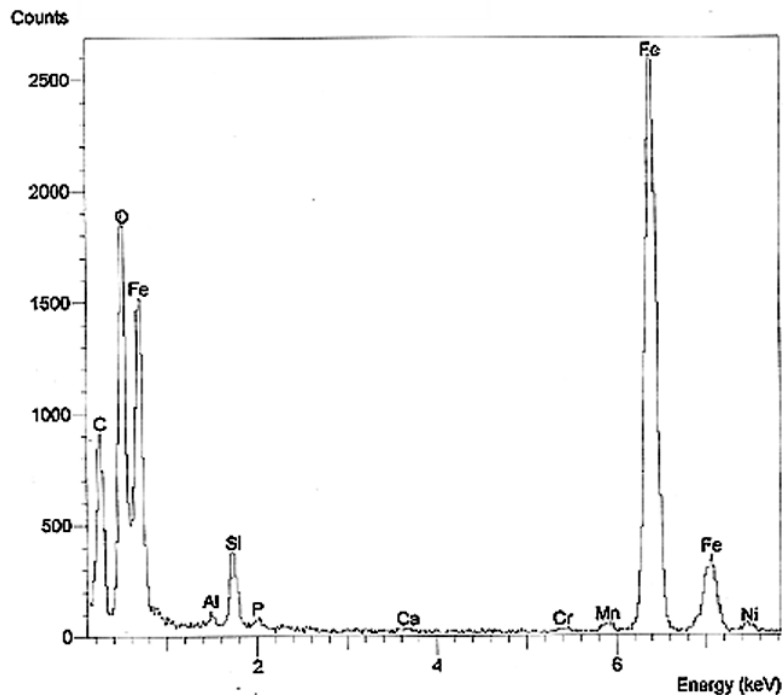


Figure 11. EDS spectrum of agglomerate adjacent to base metal in Figure 9.

2.1.3 Discussion

The TEM analysis of the corrosion layer formed on 316SS-15Zr-5U probably reveals the microstructure of the entire cross-section. The corrosion layer in this sample consists of a highly porous network of agglomerates composed of nanocrystalline grains. The thickness of the layer varied from less than 1 μm to over 10 μm thick. The thickest corrosion product came from the SEM sample mount at the metal ingot/mounting medium interface. In this region, the mounting medium was not in intimate contact with the ingot, thereby creating a crevice. Localized crevice corrosion was probably initiated at this point and further lateral growth occurred with encroachment over the surrounding ingot surface. Other regions of localized thick corrosion product were found over some of the interior ingot surface. These could be associated with underlying pits that either existed prior to testing or were generated during the test. The growth and coalescence of localized corrosion sites is probably responsible for most of the alteration layer. However, the extent to which general corrosion has additionally occurred could not be determined without examining more samples from “unreacted” appearing regions that were free of underlying ingot porosity. Zr was not detected anywhere throughout the alteration layers that were analyzed.

The composition and microstructure of the thickest corrosion layer are considerably more complex than those of the thinner alteration layers. A possible sequence of events in the formation of the layered microstructure is that the relatively uniform interfacial layer may have originated as a passivating layer that later broke down under the test conditions. While the structure of the passivating layer is currently uncertain, some reports indicate that it is initially amorphous with breakdown being associated with crystallization of the layer [13]. The crystallized state can be induced by such factors as electric fields (which are influenced by Cl⁻), mechanical stresses, or an increase in temperature. A crystallized oxide layer can be less protective than an amorphous layer because ion movement through the layer is facilitated by three-dimensional defects such as grain boundaries and dislocations. With further dissolution of the sample and outward diffusion of metal ions, precipitation from solution formed the loosely-packed agglomerates, with the nucleation of small Cr and Ni enriched agglomerates, later seen as “inclusions”, occurring first.

Many of the corrosion products identified on stainless steels consist of spinel-like structures with non-stoichiometric compositions [14, 15]. The compositional variation in the layer chemistry obtained by EDS agrees with the large compositional variations found in spinel structures. No compositional trends were observed throughout the layer, as would be expected given that the concentration of dissolved species should vary from the metal surface to the bulk solution and be reflected in the resulting composition of precipitated oxides. However, the EDS analyses are considered to be qualitative due to contamination of the underlying support and the possibility of leaching into the embedding resin prior to polymerization. For example, the source of Ca and Al, which were detected throughout the layer, is probably contamination from the testing vessel or solution. If future analysis of corroded waste forms is anticipated, then all avenues for contamination during testing and sample preparation, in addition to possible leaching into the embedding resin, will have to be removed before acquiring meaningful semi-quantitative EDS results. These results would be a beneficial adjunct to TEM electron diffraction analysis for complete phase identification.

In the present study, an immersion test with an aggressive aqueous solution containing Cl^- was used to initiate oxidation of the metal surface. The interpretation of TEM results is based on the assumption that the alteration layer has not changed with the following conditions: a) emersion from the test solution, b) embedding in a viscous epoxy medium and c) final analysis under vacuum in the TEM column. The issue of film structure alteration in the ultrahigh-vacuum of the TEM has been studied because of concerns that the vacuum may cause dehydration of the passive film. As a result, several *in situ* surface analytical techniques have been used to determine the structure of the passive film. Some studies indicate that the passive film is amorphous and/or similar to Fe hydroxides, but others indicate that the film is a crystalline spinel structure [15]. Recent studies using synchrotron x-ray scattering compared the passive film on single crystal Fe, both *in situ* and *ex situ*, to determine the oxide film structure and stability with emersion. The study concludes that emersion did not affect the film structure [16]. These experiments did not study passive films formed under the same conditions and used different kinds of surface techniques, although the layers formed on MWF samples are expected to be stable. The low viscosity resin used to embed the layers could cause leaching of oxide constituents or the layer to swell. Proper selection of an embedding resin will require comparing resins for morphological and compositional changes in the oxide layer.

The morphology of the oxide layers bears little resemblance to the microstructures described in TEM studies that characterize alteration layers on stainless steels, most of which describe a duplex oxide layer consisting of a fine-grained inner layer and a coarse-grained outer layer. A mechanism for the growth of the double oxide layer is the formation of the inner layer by a solid state growth process and the growth of the outer layer through precipitation of metal ions [13]. The inner passive layer is usually described as being in the nanometer thickness range. The coarse-grained outer layer typically consists of large single crystals. The grain size in the present study is nanocrystalline and does not vary from the MWF/oxide interface to the surface, but agglomerates (formed in the heavily corroded areas) increase in size from interface to surface. One problem in comparing data of this nature is the large number of variables that affect layer morphology, including the alloy chemistry, exposure conditions, and surface finish. Another complicating factor is the type of analytical technique and requisite sample preparation used to characterize the corrosion layer.

Ultramicrotomy is the only TEM sample preparation technique available for obtaining complete cross sectional information. Previous TEM studies of corrosion layer have relied on ion milling and/or electropolishing to prepare parallel sections at different depths in the oxide scale. Transverse sections (or cross-sections) have been prepared by ion-milling with limited success because of the different sputtering rates of the metal, oxide, and epoxy. The importance of obtaining a transverse section can not be overestimated in microstructural characterization because structural integrity at the metal/oxide interface, oxide/solution interface and the various oxide layers is necessary to understanding the mechanism of corrosion. With a pieced together image of the alteration layer, the oxide microstructure can only be deduced and not examined directly, and complexities of the corrosion layer and its relationship with a heterogeneous substrate may be lost.

2.1.4 Summary

The TEM analysis of ultramicrotomed metal waste form corrosion products reveals the microstructure and composition of the entire corrosion layer from the metal/oxide interface to the layer surface. The extraction of corrosion products from the waste form preserves the integrity of the layer and serves to minimize or eliminate radiological concerns: because uranium was not detected in the extracted layer, sample preparation and transfer was based on procedures established for cold samples.

The following characteristics of the corrosion layer were established:

- a) The layer is porous and consists of nanocrystalline grains having a spinel-like structure. Electron diffraction identified hematite as one of the phases in the layer. The EDS results are consistent with the compositional variations found in spinel structures.
- b) Heavily corroded regions have an “interfacial” layer close to the metal, with overlying fine-grained agglomerates that increase in size toward the surface.
- c) Neither uranium nor zirconium are detected in the corrosion layer.
- d) The microstructure and composition do not depend on whether the layer overlies stainless steel or intermetallic phases.

2.2 304SS-40Zr Intermetallic

A material was made with a composition of 304SS-40Zr to represent the intermetallic phase, and TEM analysis was performed on the corrosion products and underlying base metal of a vapor hydration-tested sample. An understanding of the corrosion behavior of this material without contribution from the adjacent iron solid solutions phases will help understand the corrosion behavior of the MWF. The results of TEM analysis can be compared to the Auger electron spectroscopy (AES) results obtained from the same sample [17]. Ultramicrotomy was used to prepare the sample in order to preserve the contents and spatial relationship of surface alteration products. This sample was used as a surrogate in developing a method for ultramicrotoming radioactive MWF samples.

2.2.1 Experimental: Vapor Hydration Test, 200 °C for 56 days

Sample 304/11 was reacted in a vapor hydration test conducted at 200°C for 56 days. Prior to preparing a sample for TEM analysis, the specimen was coated with a low-viscosity epoxy so that surface corrosion products would be protected during further manipulations. After polymerization at 60°C for 24 hours, the sample size was reduced by cutting the sample in half with a low-speed saw. One half of the sample was then placed on a glass slide (corroded surface down) and embedded in epoxy again.

After polymerization, the glass slide was trimmed in order to fit on the grinding/polishing jig. The glass was mounted on the polishing jig and the sample was ground down as thin as possible. The goal was to thin the bulk metal as much as possible without breaking the sample or disturbing the oxidation layer/metal interface. This required several iterations of

grinding/polishing and re-embedding, as the bond between the epoxy and the oxidation layer was easily disrupted. When this occurred, water from the grinding/polishing operation was seen infiltrating this gap, thus rendering the sample useless for TEM analysis. After grinding away most of the bulk metal, small pieces of the sample were cut out from different locations along the surface using a razor blade. These pieces were carefully oriented and embedded in epoxy blocks for ultramicrotomy. Thin sections were 500-1000Å thick and were collected onto an electron transparent carbon substrate supported by a slotted copper grid. The sections were examined using conventional brightfield imaging and the scanning image observation device that provides a scanning transmission electron microscopy (STEM) image. The TEM/STEM imaging was augmented by EDS for compositional analysis and ED for phase identification.

2.2.2 Results

The TEM results are based on the examination of thin sections taken from several regions along the sample surface. This was necessary to provide representative TEM data and to evaluate the sample preparation technique. For each sample, three regions from the surface were selected for embedding in epoxy. If corrosion did not appear uniform across the surface, regions from distinct microstructures were chosen for embedding. From each region, three blocks were produced for ultramicrotomy. Each block contained a small piece of the corrosion layer with a small amount of underlying base metal. From each block, approximately 20-30 serial thin sections were obtained and collected onto two carbon-coated Cu-grids. To evaluate section quality, at least one grid from each block was examined in the TEM. This amounted to examining a minimum of 180 sections for each sample. Of these sections, less than 5% were deemed useable. The low percentage is due to the fact that over half of the blocks produced had sample pieces that did not have enough base metal removed during grinding/polishing. The presence of too much metal adversely affects sectioning, but polishing is a difficult and critical step in the sample preparation which, if overdone, will ruin the sample.

Figures 12A-D shows that oxidation of the intermetallic under these test conditions results in the formation of three distinct alteration layers. The top layer consists primarily of Fe and O with minor amounts of Cr and Zr. This layer appears to be continuous with localized protuberances along the surface as seen in Figures 12A and B (layer 1). The thickness of layer 1 ranged from 10-40 nm (including the protuberant growths). A detached piece of this layer, the bottom of which is seen at the very top of Figure 12D (arrow), was identified by electron diffraction analysis to be hematite (Fe_2O_3). In some regions, this iron-oxide layer appears to consist of two different grain sizes. This is somewhat apparent in Figure 12D, where the top-most layer appears to consist of larger grains than the underlying iron-oxide. The regions are too small to obtain selected area electron diffraction data, but could indicate the presence of different Fe phases. Underneath the iron oxide layer is a uniform amorphous layer (layer 2) consisting primarily of Zr and O with varying amounts of Cr (up to ~17 atomic percent), Fe (up to ~19 atomic percent), and Ni (trace amounts). The thickness of this layer is approximately 20 nm. The layer was too thin to obtain a selected area diffraction pattern without contributions from adjacent structures. A microdiffraction pattern generated from within the layer showed only diffuse rings, which indicates the structure is amorphous. This is presumably ZrO_2 , as most studies regarding the oxidation of zirconium alloys, including ZrFe_2 intermetallic precipitates in

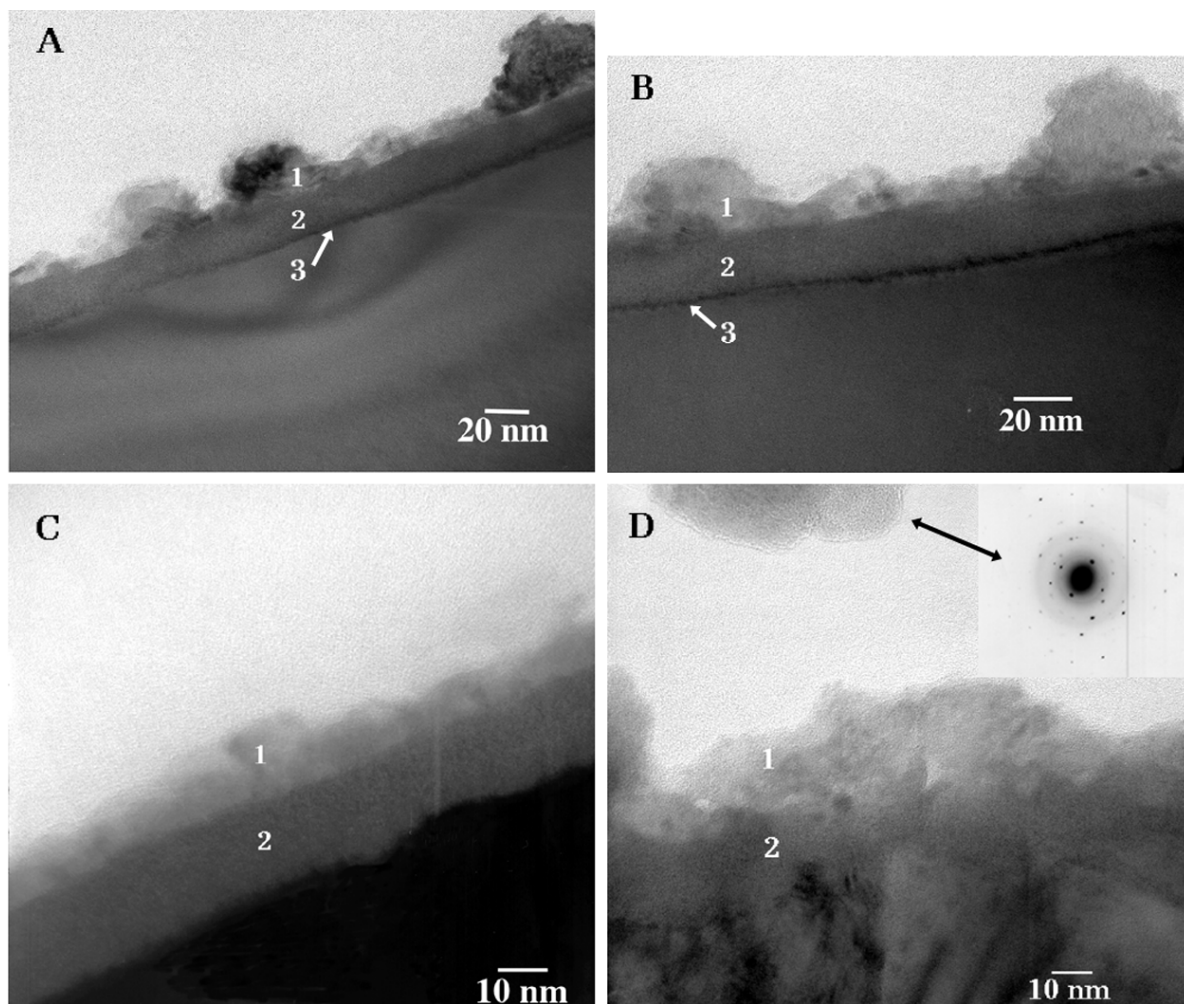


Figure 12. Surface layers from different locations on 304SS40Zr vapor hydration tested sample. Layer 1 consists of Fe-O compounds, Layer 2 is presumably an amorphous ZrO_2 layer with varying amounts of dissolved Fe, Cr and Ni, and Layer 3 consists primarily of Fe and Zr with a 1:1 ratio of Cr and Ni (10 at.%).

Zircalloys, describe the initial formation of a ZrO_2 layer [12, 18]. Given the large concentration variation of Fe and Cr within this layer, it may be that small crystallites form when those elements are present in concentrations that exceed solubility limits in ZrO_2 . Previous high resolution TEM examinations of a ZrO_2 layer revealed the existence of widely dispersed nanocrystals [11].

A very thin layer (layer 3) lying below the ZrO_2 layer is Ni-enriched and Cr-depleted in relation to the rest of the sample. This is seen as a dark line in Figures 12A and B. The Cr:Ni ratio is ~ 1 in this thin layer and < 1 in both the bulk intermetallic and overlying ZrO_2 layer. The average composition of the layer is Cr ~ 10.8 , Fe ~ 46.8 , Ni ~ 10.3 , and Zr ~ 31.7 , based on several individual spot analyses in TEM mode. This layer might represent the C36 phase, based on a comparison of these EDS results with the SEM EDS results obtained by Keiser, et al. [9]. In their study, the

Cr:Ni ratio of the C36 polytype was reported to be ~1.5. The thin dark line that represents this layer was not always observed in the TEM image. However, later STEM analysis through a region where this layer was not visible provided compositional confirmation of its existence. The results of STEM compositional analysis are shown in Figures 13A and B. Figure 13A shows the line of analysis on the STEM image. This line extends for 0.463 μm , starting outside the sample surface and ending in the bulk intermetallic. Forty spots along this line were analyzed with EDS. The results were batch analyzed so that a semi-quantitative plot of concentration (Atomic %) vs. location (Displacement) could be generated. Figure 13B shows the STEM linescan plot. (There is a small discrepancy between the scan length and the abscissa in Figure 13B.)

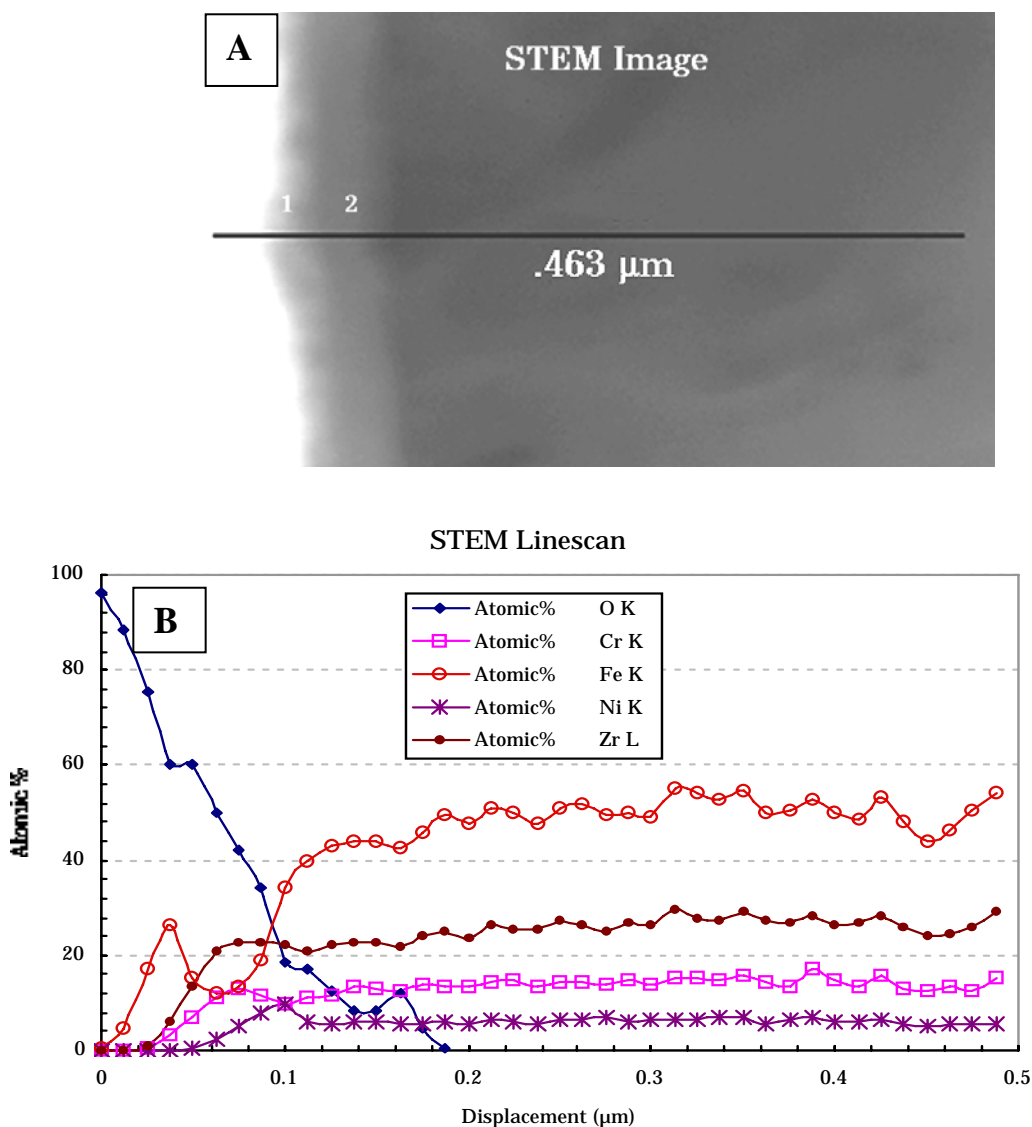


Figure 13. A) STEM image showing line of point analyses. The point analyses advanced from left to right. The layers are marked 1 and 2 and represent the layers in the TEM image (Figure 12C). B) STEM linescan plot.

The data show a correlation between the microstructure and the composition trends of the STEM linescan analysis. The microstructure consists of three layers: a top iron oxide layer with minor to trace amounts of Cr and Zr (corresponding to layer 1 in Figure 12A), a "middle" zirconium oxide layer with varying amounts of Cr and Fe (corresponding to layer 2 in Figure 12A), and a thin "bottom" layer that is Ni-enriched and Cr-depleted in relation to everything else (corresponding to the interface between layer 2 and the bulk labeled as layer 3 in Figures 12A and 12B). The Ni:Cr ratio is 1 in layer 3. It should be noted that the spot size in the STEM mode is larger than the smallest spot sizes available in TEM mode. This could result in overlap of spectral data from one point to another. For instance, O is detected in the "bottom" layer (layer 3) by the STEM analysis, but not in the TEM analysis. It is likely that the O detected by STEM analysis is a contribution from the overlying ZrO₂ layer. Approximate compositions for the layers shown in Figure 12A and intermetallic phase in Figure 12B are given in Table 1.

Table 1. EDS Results from STEM Linescan Analysis (at.%)

Area	Fe	Cr	Ni	Zr	O
Top (1)	27	2	-	5	62
Middle (2)	12	12	<2	23	44
Bottom (3)	36	10	10	22	16
Intermetallic	53	12	6	27	-

2.2.3 Discussion

The results of this study show that corrosion of the ZrFe₂ intermetallic under the vapor hydration test conditions resulted in three distinct layers: 1) an outer iron oxide layer with trace to minor amounts of Cr, Ni and Zr, 2) an inner amorphous ZrO₂ layer with varying amounts of Fe, Cr, and Ni, and 3) a thin layer consisting of Fe, Zr, Cr, and Ni (with a Cr-to-Ni ratio of 1) that is Ni-enriched and Cr-depleted in relation to the rest of the sample.

The development of a three-layer structure can be explained with the aid of previous oxidation studies of zircaloy alloys [12]. Included in these studies is the oxidation behavior of the Zr(Fe/Cr)_{2+x} intermetallic precipitates. The precipitates are present as the hexagonal C14 and cubic C15 type Laves phases that also comprise the intermetallic structure in the metal waste form. Consequently, these studies are helpful in understanding corrosion behavior of the MWF.

During the initial oxidation of zirconium alloys, a thin layer of ZrO₂ forms over the entire surface, including any exposed intermetallic precipitates. A study of Zircaloy-2 oxidized in steam at 400°C showed that an oxidized intermetallic particle close to the oxide/environment interface had a similar composition and microstructure as the vapor-hydration tested intermetallic [18]. The STEM analysis shows an outer layer of iron-oxide followed by a layer composed of Zr and O. An interesting feature of the outer iron-oxide layer is the presence of protuberant growths that appear identical to those found in the outer layer of the vapor-hydration tested intermetallic. This suggests that corrosion mechanisms are similar in the different oxidation environments.

Thermodynamic considerations can be used to explain the order of layer appearance. During the initial stages of oxidation in zircaloy alloys, the preferential oxidation of zirconium occurs first, forming a thin layer of ZrO_{2-x} . This occurs because the effective oxygen partial pressure required for zirconium oxidation is lower than that required for oxidation of Fe, Cr, or Ni. At a later stage, Fe diffuses through the ZrO_{2-x} layer, and forms iron oxides over the surface. It is not clear if Fe is in the metallic or oxidized state during this migration. Previous high resolution TEM analysis of the corroded intermetallic phase [11] shows small crystallites uniformly dispersed throughout this amorphous layer. Presumably, these crystallites contain the Fe, Cr, and Ni that are detected by EDS analysis of the layer. Although Cr_2O_3 has been reported to form during corrosion at high temperatures ($>400^\circ\text{C}$), Cr_2O_3 was not detected in the sample reacted under the vapor hydration test conditions (200°C).

The STEM analysis provides a nice format for comparison with the AES analysis performed on the same sample [17]. The oxide thickness from the AES results, based on the sputter rate of stainless steel, is estimated to be ~ 40 nm. The oxide thickness in the present study ranges from 30-60 nm due to the non-uniform thickness of the iron oxide layer. Ignoring the large protuberant growths along the surface gives an average oxide thickness between 28-34 nm (Figure 12C), which is in good agreement with the AES value.

A comparison of the STEM analysis with the AES analysis shows similar trends in Fe, O, and Zr, but with significant differences in the absolute elemental concentrations. Both analyses show a top layer rich in Fe and O, but the AES plots show a value of ~ 10 at.% Cr while the STEM plot shows only trace amounts of Cr. No more than 1.3 at.% Cr was found in any of the individual spot analyses of several different areas of the iron-oxide layer. The larger scan distance of the STEM linescan shows trends in the Cr and Ni content that occur beyond the depth of the AES concentration profile. An interesting observation is the behavior of Ni and Cr. In going from the oxide surface to the bulk metal, Ni is not detected in the iron oxide layer, but is detected (at <2 at.%) in the zirconium oxide layer. Ni peaks at ~ 10 at.% right at the oxide metal interface and then rapidly declines to a steady concentration of ~ 6 at.%. The Cr concentration appears to reach a minimum value congruent with the maximum value for Ni. Table 2 compares the compositional data obtained by STEM and AES.

There are several factors to consider when comparing the AES results to the STEM results. The techniques are very different. In AES profiling, energetic argon ions at 1-5 keV are used to sputter the surface, followed by AES for compositional identification. Sputtering is usually done continuously, with AES performed in cycles on the sputtered surface. Uncertainty in the AES depth profile may result from uncontrolled depth resolution and differential sputtering rates across the surface. In addition, the estimation of oxide thickness as a function of time is based on the sputtering rates of stainless steels. On the other hand, the STEM linescan results are obtained from a cross-section of the alteration layers and are thus very specific to the referenced STEM image. The image provides a more accurate estimate of oxide thickness than the AES

Table 2. Elemental Compositions Measured with STEM and AES (at.%)

Layer ^a	Fe	Cr	Ni	Zr	O
	STEM/AES	STEM/AES	STEM/AES	STEM/AES	STEM/AES
Top (1)	27/28	2/10	-	6/2	60/54
Middle (2) ^b	12/24	12/7	<2/3	23/12	50/54
Bottom (3)	36/ NA ^c	10/NA	10/NA	23/NA	16/NA
Intermetallic	53/56	12/16	6/4	27/21	NA

^aLayer identification corresponds to layers 1, 2 and 3 shown in Figure 12A and B.

^bConcentrations measured at 26 nm (2 minutes) on the AES plot

^cNA = not analyzed

profile and provides microstructural detail at the TEM level. The compositions measured by AES are more surface-sensitive than those measured by STEM, and the two techniques are complimentary.

2.2.4 Summary

The TEM/STEM analysis of the 304SS-40Zr intermetallic material that was reacted in a vapor hydration conducted at 200°C for 56 days reveals three distinct alteration layers: 1) an outer iron oxide layer with trace to minor amounts of Cr, Ni and Zr, 2) an inner amorphous ZrO₂ layer with varying amounts of Fe, Cr, and Ni, and 3) a thin layer consisting of Fe, Zr, Cr, and Ni. This thin layer has a Cr:Ni ratio of 1 and is Ni-enriched and Cr-depleted relative to the rest of the sample. Hematite (Fe₂O₃) was identified by electron diffraction within the topmost Fe-O layer. The bottom thin layer might represent the C36 Laves polytype, based on chemical composition analysis.

An advantage of using ultramicrotomy to prepare tested samples is the preservation of the layered structures. Attempts to ion-mill these samples did not successfully retain all the layers. The disadvantage of ultramicrotomy is the large deformation produced in the underlying base metal. This often impedes meaningful electron diffraction analysis of the base metal, particularly for the Laves intermetallic, as single crystal structures are rarely encountered. The polycrystalline nature of the ultramicrotomed intermetallic does not permit distinction of the Laves C14 (hexagonal) and C15 (cubic) polytypes. It is uncertain if the ultramicrotome is breaking up grains. The large number of unusable sections necessitated further attempts to improve section quality of subsequent samples.

A comparison of the STEM analysis with previously performed AES analysis shows similar trends in Fe, O, and Zr, but with significant differences in absolute elemental concentrations. Oxide layer thickness is estimated at ~40 nm with AES and ~30-60 nm with STEM. The thickness range from STEM analysis takes into consideration the large surface protuberances in the top-most iron oxide layer. Excluding these protuberant growths, the average oxide layer thickness is between 28 and 34 nm. The AES results indicated the presence of a layered oxide structure, but did not distinguish the microstructures and compositions of the "middle" and very thin "bottom" oxide layers that were detected by STEM analysis.

2.3 316SS-15Zr

The nominal MWF composition will include 15 mass% Zr. TEM analyses were performed on the corrosion products and underlying base metal of a vapor hydration tested 316SS-15Zr MWF sample. The vapor hydration test was conducted at 200°C for 365 days. Previous TEM analysis of a vapor hydration tested intermetallic (ZrFe_2) 304SS-40Zr sample (see Section 2.2) revealed the presence of an amorphous Zr-oxide layer over the intermetallic. Knowing that this layer forms over the intermetallic phase can serve to locate regions of intermetallic phase, which is not distinguishable from the steel phases based on microstructure alone.

2.3.1 *Experimental: Vapor Hydration Test, 200 °C for 365 days*

A sample of the MWF base composition, 316SS-15Zr, was subject to a vapor hydration test at 200°C for 56 days. The sample was prepared for TEM analysis following the protocol described in section 2.2.1, but with some modifications intended to reduce sample preparation time and improve section quality. More base metal was removed during the grinding step than was removed from previous samples. This step was done only once, rather than repeating it several times until the base metal was sufficiently thinned. After grinding the bulk metal, small pieces of the sample were cut out from different locations along the surface using a razor blade. These pieces were carefully oriented and embedded in epoxy blocks for ultramicrotomy. The sample pieces were embedded with the transverse section of the MWF, i.e., the corroded surface and base metal, perpendicular to the block surface. After polymerization of the epoxy, the sides of the block were filed down using a polishing wheel. By doing this, the reacted surface and base metal were gradually reduced to a point. The block was re-embedded and polymerized for 24 hours.

Thin sections ranged from 50 to 100 nm thick and were collected onto an electron transparent carbon substrate supported by a copper slotted grid. The sections were examined conventional brightfield imaging augmented EDS for compositional analysis and ED for phase identification.

2.3.2 *Results and Discussion*

Previous SEM examination of the entire sample revealed relatively large regions of localized corrosion. In these regions, there was a greater build-up of corrosion products over the steel phases than over the intermetallic phases. Figures 14A-D show iron oxide corrosion products overlaying the steel phase. The corrosion products consist of an iron oxide layer that is ≤ 20 nm thick that covers most of the steel surface. In some areas, the iron oxides appear as fine grained agglomerates, as seen in Figure 14D. Other regions along the steel surface appear to be pitted, as seen in Figure 14B, with the pits filled with a fine grained agglomerate of iron oxides. It is not known if the pits were pre-existing or formed during testing. The corrosion products were Cr-rich in comparison to the bulk metal, where the Cr concentration is approximately one-third the concentration of Fe. Table 3 shows the EDS analysis results for the surface corrosion products and underlying steel phase. Although Zr is present in most corrosion products, from trace levels to ~10 at. %, it is not present in the underlying steel phases.

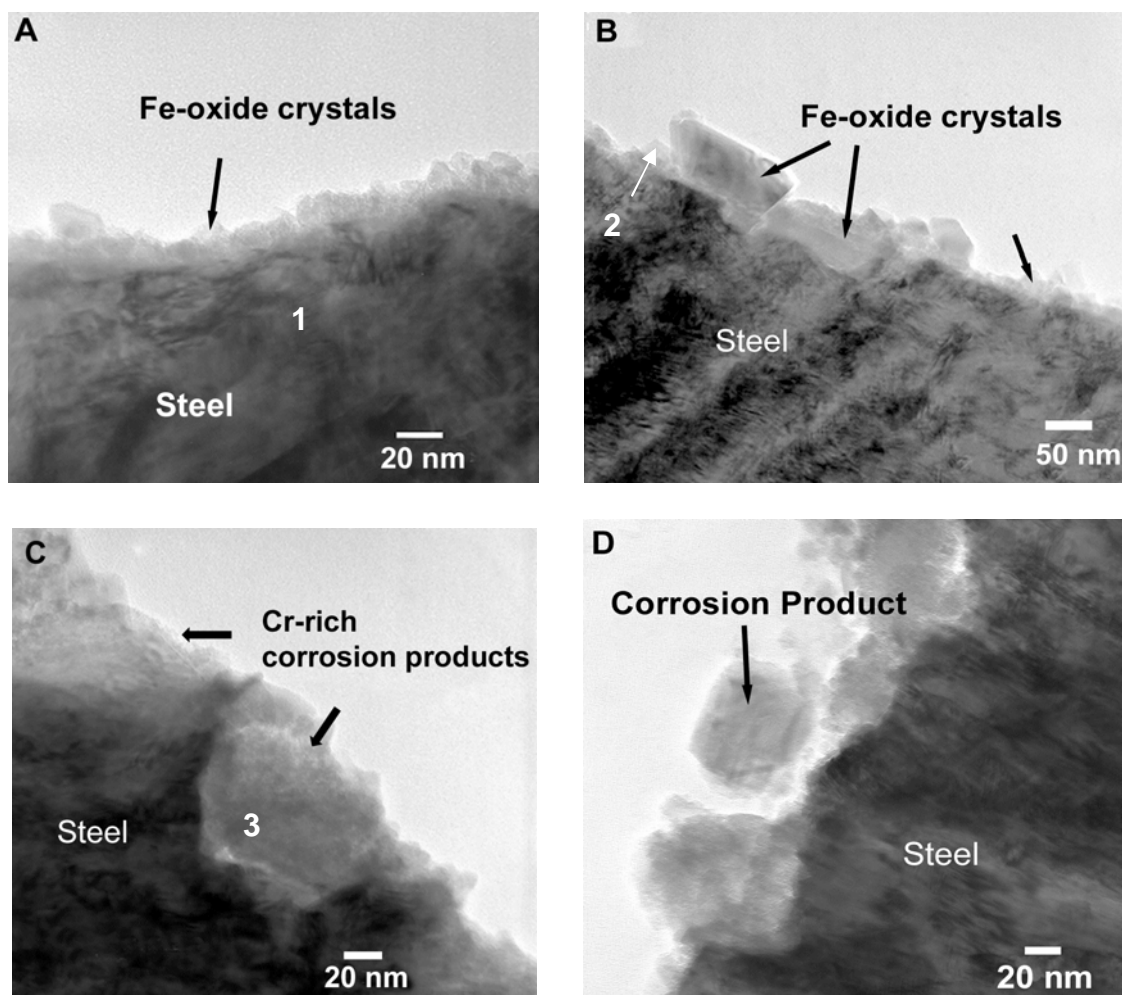


Figure 14. Cross-sections of vapor hydration tested sample (316SS-15Zr) showing surface corrosion products formed over the steel phase. Figure C shows Cr-rich corrosion products that appear to be in pits. Areas of EDS analysis are numbered.

Table 3. EDS Analysis of Corrosion Products and Underlying Steel (at.%)

Area	O	Cr	Mn	Fe	Ni	Zr	Mo
1 (steel)	-	23.8	1.5	68.9	3.9	-	1.8
2	64.0	16.6	0.8	7.7	0.3	10.5	-
3	82.7	8.6	0.3	6.2	1.5	-	0.7

The corroded intermetallic surface consists of patchy fine-grained iron oxides overlying an amorphous layer consisting of Zr, O and small amounts of Fe and Cr. The layer is ~50-70 nm thick and is covered with fine-grained iron oxide crystals. This layer ends near the steel/intermetallic interphase boundaries, as seen in Figure 15A and B. The Zr-oxide layer appears to encroach into the steel phase surface for a short distance and then ends abruptly. This

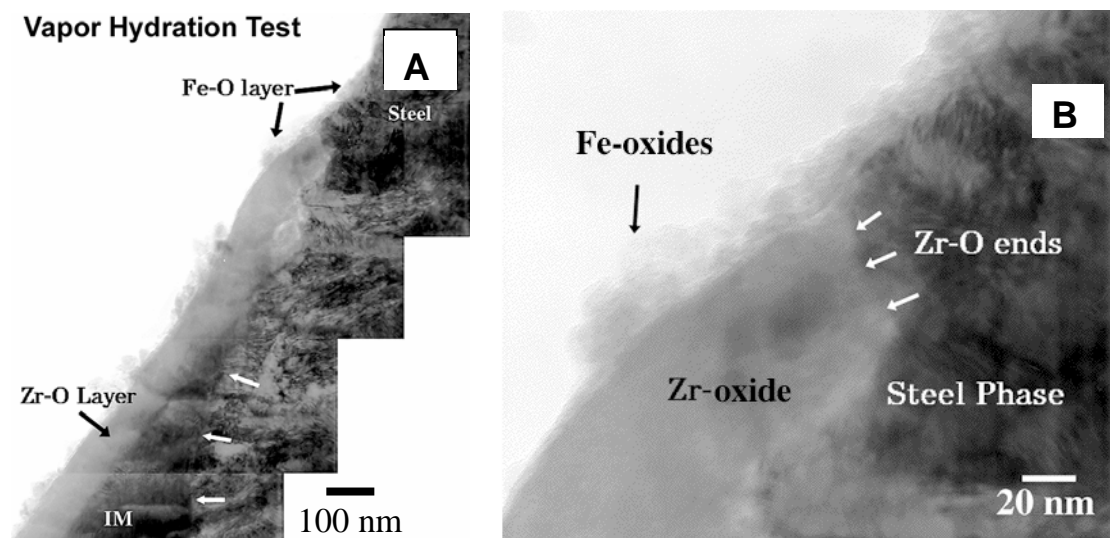


Figure 15. Corrosion products formed on the MWF intermetallic phase. Zr-oxide layer over the intermetallic phase ends at steel/intermetallic phase boundary: (a) white arrows point to the intermetallic (IM)/steel phase boundary and (b) white arrows show where the Zr-O layer ends.

type of layer was also observed in the vapor hydration tested 304SS-40Zr sample reacted for 56 days at 200°C (see section 2.2). Table 4 shows EDS analysis results from the uniform amorphous layer in Figure 15B.

Table 4. EDS Analysis of Alteration Layer (at.%)

Area	O	Cr	Mn	Fe	Ni	Zr	Mo
1	38.27	6.20	-	11.88	-	43.64	-

The same thermodynamic considerations used to explain the formation of this layer in previously analyzed MWF samples apply to this sample. Because the MWF is a eutectic microstructure consisting of equal amounts of intermetallic and steel phases, the adjacent steel phases are probably a major Fe-contributor to the iron oxides that form over the intermetallic phases.

2.3.3 Summary

The TEM analysis of the 316SS-15Zr MWF sample that was vapor-hydration tested at 200°C for 365 days reveals an outer iron oxide layer with trace to minor amounts of Cr, Ni, and Zr, and an inner amorphous ZrO₂ layer overlying the intermetallic phases that contained minor amounts of Fe and Cr. The iron oxides generally appear as distinct crystals that form either as a relatively uniform layer over the steel phases or as fine-grained aggregates on the surface or in surface pits. The fine-grained aggregates appeared to be present along a more irregular surface in comparison to the surface covered with the larger distinct crystals. The fine-grained agglomerates had a

higher Cr-to-Fe ratio than the steel. Trace levels of Zr (<10 at.%) were detected in the iron oxides overlying both the steel and intermetallic phases.

An advantage to using ultramicrotomy to prepare tested samples is the preservation of the layered structures. Attempts to ion-mill these samples were unsuccessful in retaining all the layers. The modification in sample preparation technique resulted in preservation of layered structures over the steel and intermetallic phases and reduced sample preparation time.

2.4 316SS-15Zr-0.5Ag-1.5Pd-2Ru

Noble metals were added to the base 316SS-15ZR composition as surrogates for noble metal fission products that will be present in actual MWF products. The noble metal composition in the actual MWF will consist of ~ 0.2 – 0.6 wt. % Ru, 0.1 wt. % Pd, and ppb levels or lower of all other fission products. TEM analysis was performed on the corrosion products and underlying base metal of an immersion tested MWF sample consisting of the base metal composition with the following added noble metals: 0.5 Ag, 1.5 Pd and 2.0 Ru. The sample was immersion tested in deionized water at 200°C for 91 days. Previous immersion tests at 90°C were not adequate for studying MWF corrosion, therefore, tests had been run at higher temperature to accelerate corrosion so that the disposition of the noble metals and their effect on the MWF microstructure and phase composition could be studied.

2.4.1 Experimental: Immersion Test, 200 °C for 91 days in deionized water

A sample consisting of the MWF base composition 316SS-15Zr with added Ag, Pd, and Ru was immersion tested in deionized water at 200°C for 91 days. The sample was prepared for TEM analysis following the protocol described in section 2.3.1. Thin sections ranged from 500-1000 Å thick and were collected onto an electron transparent carbon substrate supported by a copper slotted grid. The sections were examined using conventional brightfield imaging augmented by EDS for compositional analysis and ED for phase identification.

2.4.2 Results and Discussion

Leachate solution analysis to determine elemental composition was obtained by ICP-MS. Elemental concentrations were used to calculate the normalized mass loss, in g/m², according to the following equation:

$$NL(i) = \frac{\{C(i) - C^{\circ}(i)\} \times V}{S \times f(i)} \quad (1)$$

- NL(i) = normalized mass loss based on element i (g/m²)
- C[°](i) = initial concentration of element i in leachant (g/m³)
- C(i) = concentration of element i in test solution (g/m³)
- V = volume of leachant (m³)
- f(i) = mass fraction of element i in sample
- S = surface area of the sample (m²)

Normalization to the S/V ratio used in a test and to the mass fraction of each element allows direct comparison of the releases of different elements from different materials under different test conditions. Table 5 shows the normalized elemental loss values for the tested MWF monolith. The test data shown here was obtained in tests run in titanium vessels. These solution results indicate that elemental losses are small under these test conditions and that the noble metals Ag and Ru are released into solution during corrosion.

Table 5. Normalized Mass Loss (g/m^2) of Elements from 316SS-15Zr-0.5Ag-1.5Pd-2Ru in Immersion Test in Deionized Water at 200°C for 91 Days

Fe	Cr	Ni	Zr	Ag	Pd	Ru	Mo	Mn	Co	Cu	V	Si
BD ^a	0.21	0.65	BD	1.22	BD	4.6E-4	1.1E-3	0.01	0.55	0.50	BD	10.6

^aBD = concentration was below detection level.

Previous SEM examinations did not reveal an obvious corrosion layer or corrosion products. In contrast to the vapor hydration tested samples discussed in the previous sections, localized corrosion was not evident and the corrosion layer thickness was nearly uniform. Figure 16 shows the oxidation layer that formed over the steel phase. This layer varied in thickness from 50 nm to 250 nm and appears to consist of an outer coarse-grained layer (labeled 1 in Figure 16) and an inner fine-grained layer (labeled 2 in Figure 16) that is ~25-70 nm thick. Zr was detected in both layers, usually at <10 atomic percent. This was also the case in the previous study of a vapor hydration tested MWF sample consisting of the base MWF composition (Section 2.3). Noble metals were detected in both layers.

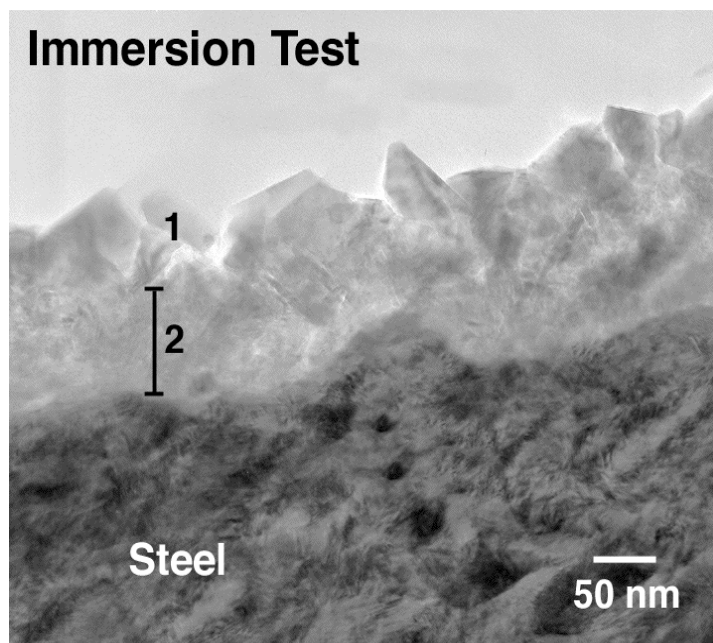


Figure 16. Corrosion products formed on the MWF steel phase from immersion test at 200°C for 91 days.

Table 6 shows EDS results for the oxidation layers form over the steel phase. Layer 1 compositions are from areas similar to that shown in Figure 16 labeled 1. Layer 2 compositions are from areas similar to that shown in Figure 16 labeled 2. The base metal composition was taken from an area immediately below layer 2.

Table 6. EDS Analysis of Corrosion Products Over Steel Phase, (at.%)

EDS Area	O	Cr	Mn	Fe	Ni	Zr	Ru	Ag	Mo	Pd
Layer 1	51.4	0.4	1.1	31.0	1.4	6.9	0.3	0.2	-	7.4
Layer 2	47.1	0.5	1.6	24.4	-	24.0	1.3	-	-	1.1
Steel Phase	-	25.0	1.5	67.9	3.5	-	0.7	-	1.5	-

Figure 17 shows the oxidation layers that formed over the intermetallic phase. There appear to be three layers with a combined thickness of ~230 nm. The layer thicknesses did not vary significantly across the sample. The topmost layer 1 consists of distinct crystals containing mainly Fe and O, with a small amount of Zr. The middle layer 2 is a finer-grained material with a composition similar to that of layer 1. Layer 3 is amorphous and ~50 nm thick. The results of EDS spot analyses conducted at the approximate locations of the labels in Figure 17 and in the bulk intermetallic phase are given in Table 7. It was difficult to distinguish layer 2 from layers 1 and 3 on the TEM phosphor viewing screen, therefore the EDS analysis of layer 2 probably includes contributions from layers 1 and 3.

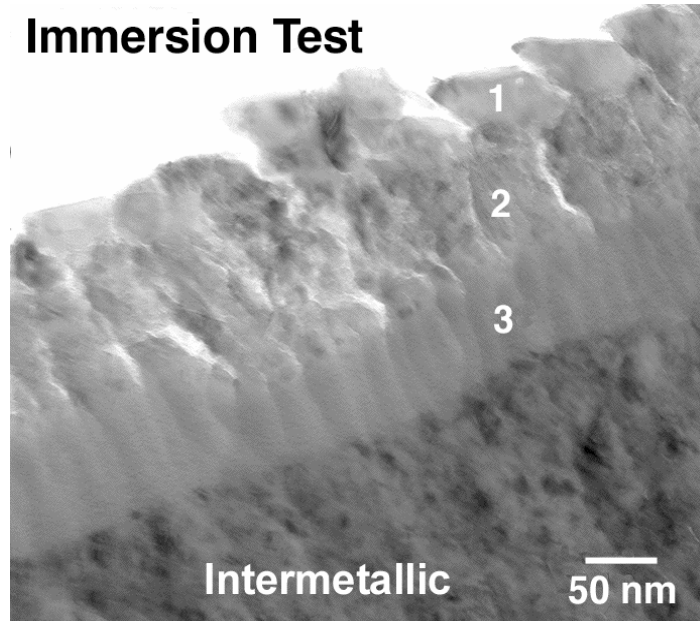


Figure 17. Corrosion products on the MWF intermetallic phase from immersion test at 200°C for 91 days.

Table 7. EDS Analysis of Corrosion Products Over Intermetallic Phase (at.%)

EDS Area	O	Cr	Mn	Fe	Ni	Zr	Ru	Ag	Pd
Layer 1	52.9	0.9	0.1	41.2	1.0	3.3	0.6	-	-
Layer 2	55.7	0.6	0.1	31.3	2.4	9.0	0.3	0.6	-
Layer 3	60.0	0.1	0.6	18.7	0.8	18.4	-	0.1	1.2
Intermetallic	-	4.8	0.8	45.6	18.0	25.1	1.9	0.9	3.0

Figures 18A and 18B show the results of an EDS linescan taken over a 5- μm distance starting in the underlying intermetallic phase and passing through the oxidation layers. The inset in Figure 18B shows the scan path on the image. Figure 18A shows EDS results for the base components and Figure 18B shows the distribution of noble metals. Figure 18B shows that the noble metals Pd and Ru decrease from bulk levels at the linescan 2 μm position to much lower levels in the corroded surface layer beyond the linescan 3 μm position.

2.4.3 Summary

The TEM analyses of the 316SS-15Zr MWF doped with noble metals and immersion tested in deionized water at 200°C for 91 days reveal a duplex iron oxide structure over the steel phases, and relatively uniform oxidation consisting of three distinct layers over the intermetallic phases. The top and middle layers consist of iron oxides, coarse grains on the top and finer grains in the middle. The bottom layer (in contact with the intermetallic) consists of a single amorphous non-stoichiometric Zr-oxide layer.

The EDS results, collected both as a linescan and as individual spot analyses, indicate that noble metals are present in the corroded surface, but at levels lower than in the bulk. The spot analyses were obtained at a longer acquisition time than the linescan analysis to enhance the collection statistics of trace elements. These spot analyses confirm the trend seen in the EDS linescan analysis. Palladium was detected at 7.4 atomic % in the top-most iron oxide layer of the steel phase (see Table 6), but was not detected in the steel phase itself. It was not detected in the test solution, suggesting that all of the Pd released from the intermetallic phase as it corroded was sequestered in the iron oxide layers that formed over the steel phases. Interestingly, Pd was not detected in the two top-most iron oxide layers that form over the intermetallic phases, even though it is detected in the bulk intermetallic phase and in the adjacent oxide layer 3. Ag and Ru, which are also depleted in the layers formed on the intermetallic, were detected in the solution. The ICP-MS results also show that elemental releases are small at 200°C.

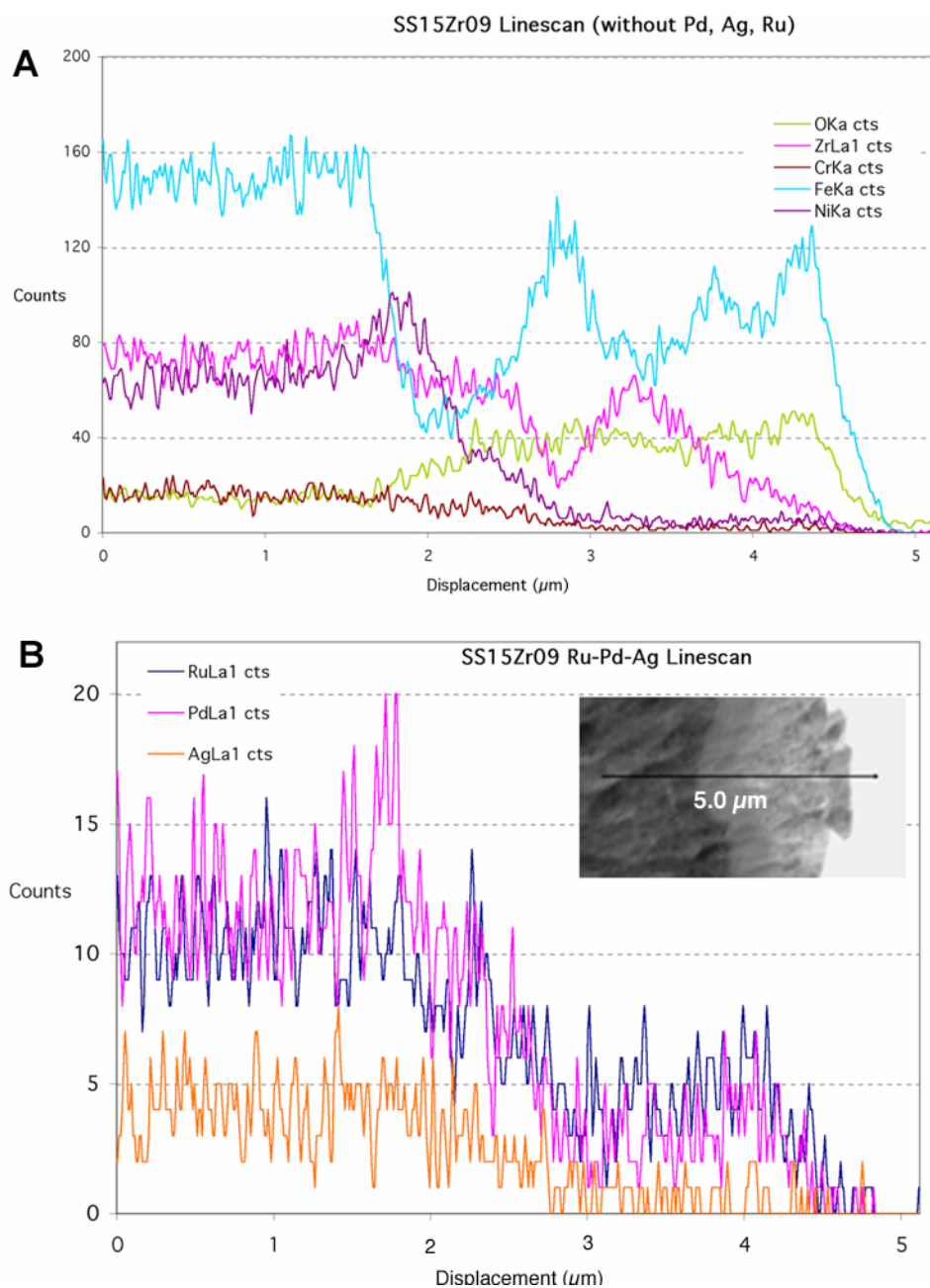


Figure 18. Results of STEM linescan for (A) base metal components and (B) doped noble metals (see micrograph insert in above plot for line location). The linescan analysis proceeded from left to right. Elemental analysis along this line shows the presence of noble metals in the corrosion layers.

2.5 316SS-15Zr-11U-0.1Pd-0.6Ru-0.3Tc and SS-15Zr-2U-1Nb-1Rh-1Ru-1Tc

TEM analyses were performed on the corrosion products and underlying base metals of two MWF samples consisting of the base 316SS-15Zr composition with the following additions: 11U-0.6Ru-0.3Tc-0.1Pd (referred to as Sample 61) and 2U-1Nb-1Rh-1Ru-1Tc (referred to as Sample 31). The noble metals were added as surrogates for noble metal fission products that will be present in the actual MWF. Uranium will be the most abundant actinide in the MWF, at ~1 - 11 wt. % and, for testing purposes, also serves as a surrogate for Pu and Np (both will be present in the MWF at ppm levels). Uranium exists in elemental form throughout the intermetallic phases with a preference for the C15 polytype. Technetium will be present at ~0.1 – 0.3 wt. % in the MWF and is important to study because it is a relatively long-lived fission product that is mobile in an aqueous environment. Tc is distributed throughout the MWF, but favors the ferrite and austenite steel phases. The purpose of tests with these materials was to identify the fate of the noble metals as the MWF corrodes.

2.5.1 Experimental: Immersion Tests, 90 °C for 400 and 700 days

Samples 61 and 31 were immersion tested at 90°C for 400 days and 700 days, respectively. The leachant used in the immersion test was simulated tuff groundwater (see [19] for details.) The samples were prepared for TEM analysis following the protocol described in Section 2.3.1. Thin sections ranged from 50 -100 nm thick and were collected onto an electron transparent carbon substrate supported by a copper slotted grid. The sections were examined using conventional brightfield imaging, EDS for compositional analysis, and ED for phase identification.

2.5.2 Results

Leachate solution analysis to determine elemental composition was obtained by ICP-MS. Elemental concentrations were used to calculate normalized mass loss values, in g/m², using Equation 1. Table 8 lists the normalized mass loss from both samples (see [19]). Immersion test results show that NL(U) is more than an order of magnitude greater than NL(Tc) for both alloys.

Table 8. Normalized Mass Loss (g/m²) of Elements in Samples 31^a and 61^b

Sample	Fe	Cr	Ni	Zr	Mo	Mn	U	Tc
Sample 31 ^a	6.5E-4	2.6E-3	<3.E-4	4.5E-3	2.4E-2	6.1E-4	1.8	8.3E-3
Sample 61 ^b	2.2E-3	2.2E-2	<3.2E-4	7.2E-2	3.4E-2	1.9E-4	0.67	3.5E-2

^a316SS-15Zr-2U-1Nb-1Rh-1Ru-1Tc immersion tested in deionized water at 90°C for 400 days.

^b316SS-15Zr-11U-0.1Pd-0.6Ru-0.3Tc immersion tested in deionized water at 90°C for 700 days.

TEM Analysis

Identification of the base metals in the TEM samples was not straightforward for either alloy, as elemental compositions from what appeared to be a base metal were not consistent with all steel or all intermetallic phase compositions. Where corrosion products were detached from the underlying base metal, the detached base metals were considered to be intermetallic phases if

they contained Zr and U, and steel phases if they lacked Zr and U but contained Mo.

316SS-15Zr-2U-1Nb-1Rh-1Ru-1Tc (Sample 31)

Figure 19A shows the corrosion products formed over what is considered to be the intermetallic phase in Sample 31. The detachment of the corrosion layer from the underlying base metal presumably occurred during thin sectioning (based on the absence of epoxy between the metal and the layer). The corrosion products consist of a porous network of agglomerates made up of nanocrystals. The results of EDS analysis of the layer adjacent to the intermetallic are shown in Table 9 as the IM layer. The thickness of this layer is ~200 nm and the layer consists primarily of Fe oxides with trace amounts of Cr, Zr, Nb, and U.

Corrosion products formed over the steel phase are shown in Figure 19B in what appears to be three layers. The topmost layer (SS Layer 1, which is barely visible) is an extensive porous network of Fe-oxide, presumably hematite, which may be up to several micrometers thick. Beneath the Fe-oxide is a layer (SS Layer 2) that consists of mainly O, Fe, and Cr, with trace amounts of Nb, Tc, Ru and U. The thickness of this layer varies from ~40-80 nm. The layer adjacent to the base metal (SS Layer 3) is ~40 nm thick and consists of Fe, Zr, Ni, Cr, and O, with trace amounts of Nb, Tc, Ru, and U. The EDS results for the layers over the intermetallic and steel phases in Figures 19A and 19B are shown in Table 9.

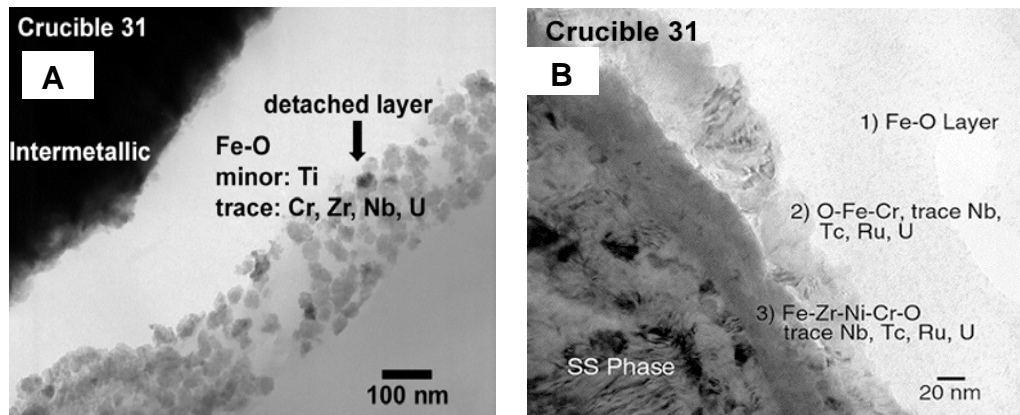


Figure 19. Corrosion products formed over the (A) intermetallic and (B) steel phases of Sample 31.

Table 9. EDS Analysis of MWF Surface Corrosion Products Over Intermetallic and Steel Phases in Sample 31, (at.%).

Area of EDS	O	Cl	Ti	Cr	Fe	Ni	Zr	Nb	Mo	Tc	Ru	U
IM Layer	86.9	0.40	0.80	0.48	10.9	-	0.41	-	-	-	-	0.07
SS Layer 1	85.6	-	-	-	14.4	-	-	-	-	-	-	-
SS Layer 2	41.3	-	-	12.5	37.1	4.12	3.11	0.38	0.80	0.32	0.14	0.25
SS Layer 3	10.8	-	-	11.7	49.3	11.2	14.3	0.74	0.82	0.02	0.23	0.79

316SS-15Zr-11U-0.6Ru-0.3Tc-0.1Pd (Sample 61)

Figure 20A shows corrosion products that formed over the intermetallic phase in Sample 61. There appears to be two distinct layers. The top layer 1 consists primarily of small-grained Fe-O agglomerates and varies in thickness to a maximum of ~40 nm. Below this layer is a uniform amorphous layer 2 that is ~20 nm thick and composed primarily of O, Fe, and Zr, with small amounts of Ni, Cr, and U. Region 3 (shown by the arrow) is at the interface between the oxide layer and bulk intermetallic phase. The region labeled 4 in Figure 20A is probably the bulk intermetallic. The results of EDS analysis of the numbered regions in Figure 20A are shown in Table 10. The concentration of noble metals in Sample 61 is representative of the actual MWF. No noble metals were detected in the corrosion products, but the concentrations may be below EDS detection limits. Corrosion products that formed over the steel phase are shown in Figure 20B. The layer is detached from the underlying base metal, which was not preserved in the thin section. These corrosion products are assumed to have formed over the steel phase based on the fact that Mo is present and U is not. The corrosion products consist of a porous network of agglomerates made up of nanocrystals. The thickness of this layer is ~100 nm, and it is an iron oxide, presumable hematite, with trace amounts of Zr, Mo, Ni, and Cr. The EDS results from this region are shown in Table 10.

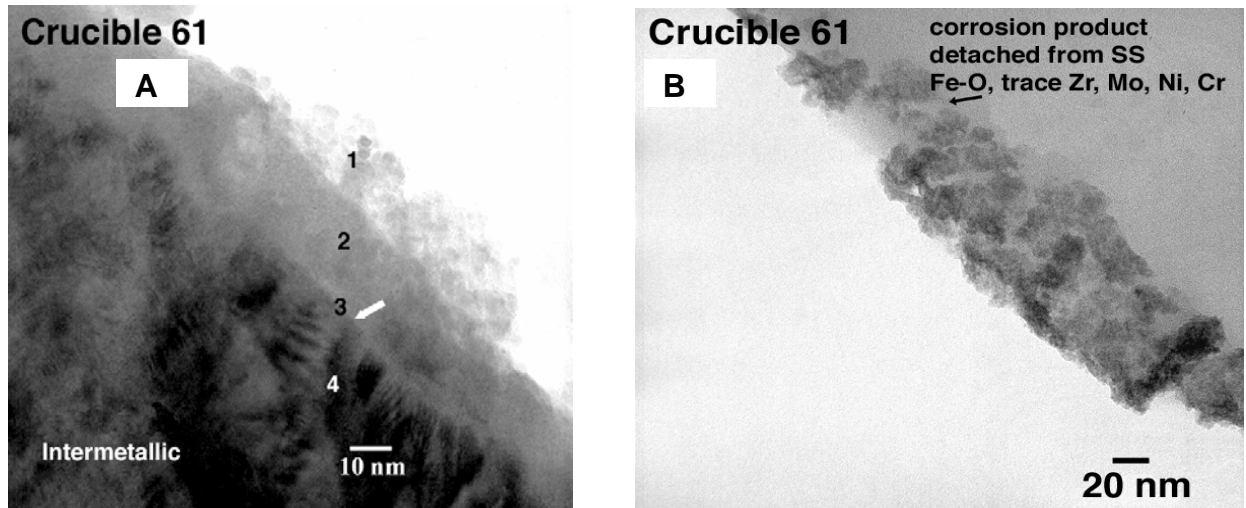


Figure 20. Corrosion products formed over the (A) intermetallic and (B) steel phases of Sample 61. Figure B shows only the detached corrosion layer that formed over the steel phase.

Table 10. EDS Analysis of MWF Surface Corrosion Products Over Intermetallic and Steel Phases in Sample 61, (at. %).

Area of Analysis	O	Cr	Fe	Ni	Zn	Zr	U
IM Layer 1 ^a	63.1	0.7	31.1	1.9	1.93	1.0	0.2
IM Layer 2 ^a	52.6	3.2	21.5	5.9	-	14.3	2.6
IM Layer 3 ^a	30.9	3.6	35.2	9.9	-	17.3	3.1
IM Layer 4 ^a	19.9	4.1	42.2	12.0	-	18.8	3.4
SS Layer ^b	90.3	0.02	9.1	0.01	-	0.3	0.3

^aSee Figure 20A.

^bSee Figure 20B.

2.5.3 Summary

The microstructure of the corroded intermetallic phase in Sample 61 consists primarily of an outer layer of small-grained Fe-oxide agglomerates that varies in thickness to a maximum of ~40 nm. Below this layer is a uniform amorphous layer, ~20 nm thick, composed primarily of O, Fe, and Zr, with minor amounts of Ni, Cr, and U. The corrosion products over the steel phase in Sample 61 consist of a porous network of agglomerates made up of nanocrystals. The thickness of this layer is ~100 nm and it is an iron oxide, presumable hematite, with trace amounts of Zr, Mo, Ni, and Cr.

Identification of the base metal is difficult when the corrosion products are separated from the base metal. This typically occurs during thin sectioning. When this happens, it is likely that the material on either side of the gap will be sectioned at different thicknesses. Usually the base metal will be sectioned at a thickness much greater than the ultramicrotome setting. The EDS analysis of the base metal may be complicated because the thickness in this region could be great enough to contain two phases, one being below the other. The resulting EDS analysis will therefore contain the elemental composition of the two phases. This could explain the somewhat unexpected findings on the corroded surface of Sample 31, namely, that the corroded intermetallic phase did not contain the ubiquitous amorphous Zr-oxide layer that is present over the intermetallic of every other corroded MWF sample examined to date. It is possible that the base metal is actually steel. For the present analyses, the most reliable result from EDS analysis for determining whether a corrosion product formed over the steel or intermetallic phase was the presence of noble metals, U, and Tc in the corrosion products.

Immersion test results show that U release is more than an order of magnitude greater than Tc release for both alloys. Both alloys show essentially the same normalized mass losses for U and for Tc. Noble metals were not detected by EDS analysis, but may have been present in amounts below detection limits. These results indicate the need for future work directed at understanding U release from the MWF. Continued improvements in sample preparation should eliminate ambiguous interpretation of microstructure and will help in relating solution results to TEM results.

2.6 316SS-15Zr-5U

TEM analyses were performed on the corrosion products and underlying base metal of a MWF sample consisting of the base metal composition with 5 wt. % added U that had been reacted in a pulsed-flow immersion test.

2.6.1 Experimental: Pulsed-Flow Immersion Test, 90 °C for >445 day

A MWF sample consisting of 316SS-15Zr-5U was reacted in a pulsed-flow immersion test in simulated groundwater at 90°C for at least 445 days. (The test was terminated after an unknown total reaction time, but the last sampling of the solution occurred after 445 days.) The test was an immersion test in which approximately 5 to 10% of the test solution was periodically removed for analysis and replaced by fresh leachant, and the test continued. The release of MWF components to solution was measured as a function of time.

The reacted sample was prepared for TEM analysis following the protocol described in Section 2.3.1. Thin sections ranged from 50 to 100 nm thick and were collected onto an electron transparent carbon substrate supported by a copper slotted grid. The sections were examined using conventional brightfield imaging augmented by EDS for compositional analysis and ED for phase identification.

2.6.2 Results and Discussion

Figure 21 shows the intermetallic phase with the typical amorphous Zr-oxide layer that has been observed to form at its surface on all tested MWF samples. Areas analyzed with EDS are labeled A (surface), B (interface) and C (intermetallic), and the results are shown in Table 11. Uranium is present in the corrosion layer at concentrations that are higher than those measured on other corroded MWF samples. The average concentration in this layer is ~6 atomic %. An unusual microstructural feature is the presence of cracks or notches throughout the layer; for example, the arrow in Figure 21 points to a discontinuity in the oxide layer that extends from the layer surface through the interface. In other regions, there appear to be cracks initiating at the surface. This was not seen in any other samples used in TEM studies and could have occurred during either the test or during sample preparation. The presence of such discontinuities in the layer may be associated with break down of surface passivation, which could have significant consequences on the long-term durability of the MWF.

2.6.3 Summary

The TEM results for the corroded intermetallic phase in a 316SS-15Zr-5U MWF sample show the typical amorphous Zr oxide layer seen in all tested MWF samples that have been examined, but with unique microstructural features that have not been previously observed. At various locations along the surface, this layer had discontinuities that ranged from small surface cracks to large gaps that penetrated to the oxide/metal interface, similar to what is seen in Figure 21. This could have implications for MWF stability in that it may be associated with passivation breakdown and points to the need for future studies aimed specifically at observing the corroded surface as the surface passivates and then breaks down.

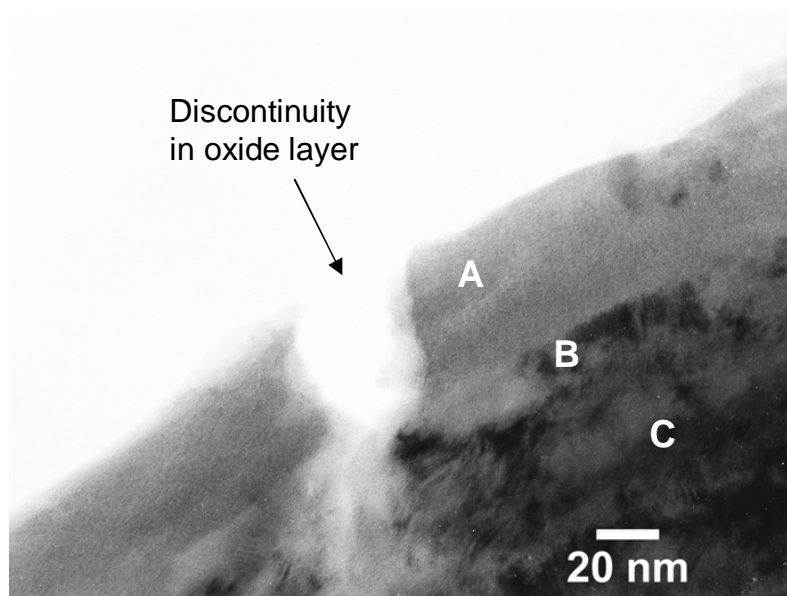


Figure 21. Corrosion layer over the intermetallic phase. Areas of EDS analysis are labeled A (surface), B (below interface) and C (bulk). Arrow points to discontinuity in the oxide layer.

Table 11. EDS Analysis of MWF Surface Corrosion Products Over the Intermetallic Phase, (at. %).

Area	O	Cr	Mn	Fe	Ni	Zr	U
A	64.7	1.8	-	12.6	5.5	10.1	5.2
B	59.4	1.2	0.6	17.9	10.8	6.2	3.8
C	--	2.0	2.0	41.2	30.4	14.2	10.2

3.0. LOCALIZED CORROSION

The TEM analyses of reacted MWF were thus far focused on general corrosion. The contribution of pores to MWF corrosion has been ignored even though they constitute a significant portion of the MWF surface. It is well known that the rates of localized corrosion, such as what is occurring over these pores, can be several orders of magnitude higher than uniform corrosion of metals. The SEM examinations of an immersion tested sample that showed relatively little surface corrosion revealed extensive dendritic and grain boundary or interphase boundary dissolution within a pore. Figure 22 is an SEM image of the immersion tested MWF sample that shows a region of extensive localized corrosion. The gouged out region was covered by a large heap of red (Fe_2O_3 and/or $\text{Fe}(\text{OH})_3$) and black iron oxides (Fe_3O_4). This was removed from the surface in order to examine the “crater” surface shown in Figure 22. Notice that the surrounding surface appears uncorroded, and scratches in the 600 grit surface finish are still visible. It is not clear if this crater was created at the location of a pre-existing surface pore or if pitting corrosion was initiated at this area, because the samples were not examined before testing.

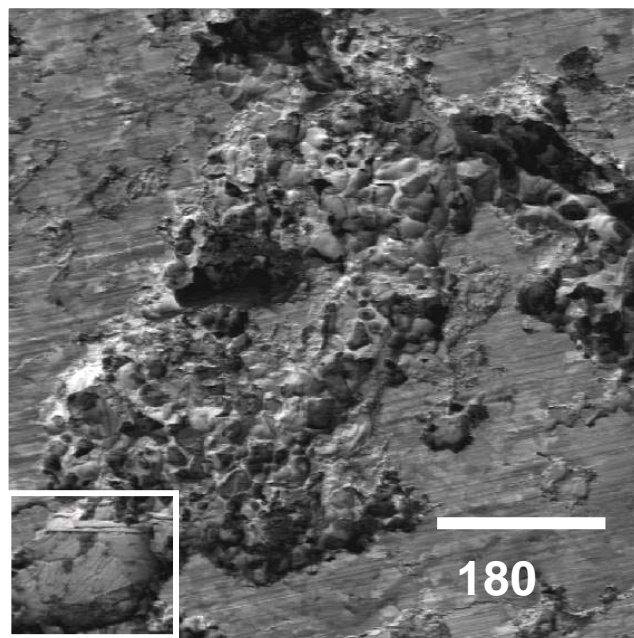


Figure 22. SEM image showing region of localized corrosion on the MWF surface.

Figures 23A and 23B show higher magnification images of an area within the crater. Both images reveal a dendritic morphology, which probably occurred during solidification and was revealed during dissolution. The deep channels are probably regions of preferential dissolution at a grain boundary or interphase boundary.

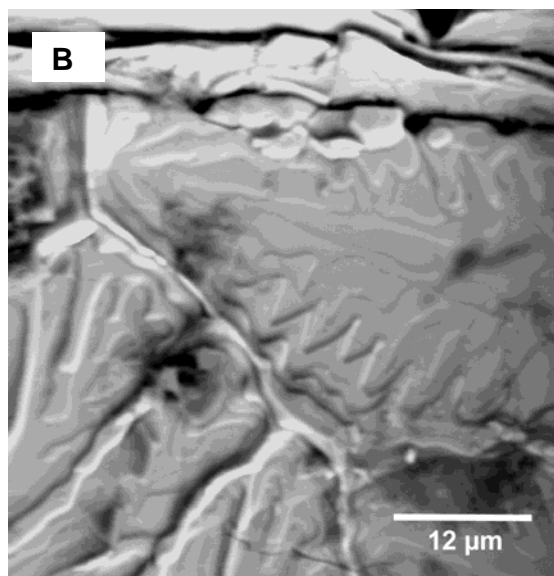
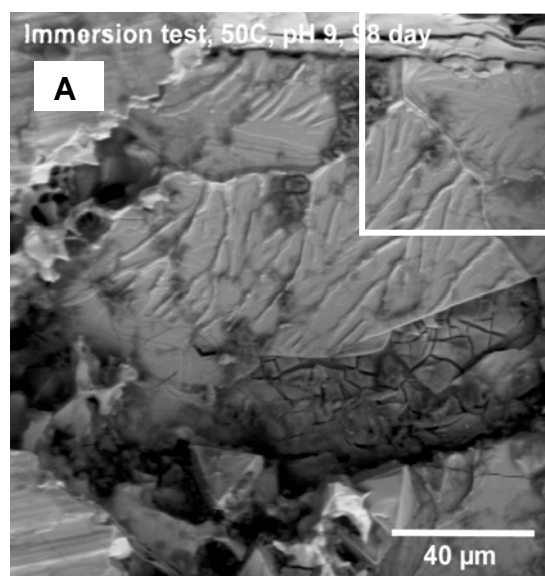


Figure 23. A) High magnification SEM image of boxed area shown in Figure 22 and B) higher magnification of boxed area in Figure 23A showing extensive dendritic and grain boundary or interphase boundary dissolution.

Because TEM analyses have established the predominance of U disposition in the cubic C15 ZrFe₂ polytype and SEM analysis shows a gradient of U concentration with the highest U concentrations at interphase boundaries, U release is probably significant during corrosion of material within the craters. This may indicate that the C15 polytype is the last polytype to solidify and is the lowest melting point constituent. Given that the C15 polytype solidifies at interphase boundaries, there is an opportunity for increased localized corrosion within these craters (pits). This represents a potentially significant route for U release and could result in U being released from regions of localized corrosion faster than occurs during uniform corrosion.

4.0. RECOMMENDATIONS FOR FUTURE WORK

The results of all TEM studies thus far show that the most effective method of sample preparation is ultramicrotomy of the reacted surface and underlying base metal. Although sample preparation methods that do not include the base metal attached to the reacted surface provide valuable insight into the alteration phases that form, they do not provide a complete picture of corrosion events. When other sample preparation methods in which the corroded surface was extracted, scraped, or scribed from the surface, complexities in the microstructure at the interface of the alteration layer and underlying substrates are likely to be missed. As the results to date show, the reacted surface of the MWF consists of both adherent oxide layers and precipitated phases. The topological and spatial orientation of structures must be retained to relate TEM results with the corrosion mechanism. This is particularly important because the MWF surface is a multi-phase eutectic with solid solution iron phases (ferrite and austenite) and several polytypes of the Laves intermetallic. The organization, location, thickness, composition, and structure of layers and precipitates and their interactions should be a principal focus of future TEM analyses.

Future TEM analyses should address the role of the corrosion layers in passivating the surface and the following issues: How do the passivating properties of the layers change with time, temperature, and pH? Under what conditions do the passivating layers break down? What is the likelihood that oxide layers will spall off the surface under changing repository environments? What phases exist on the reacted surface and what is the disposition of radionuclides in these phases? Ultimately, an understanding of the evolution of the layer structures that form during corrosion is essential because these probably determine the long-term MWF corrosion behavior. The answers to these questions will likely necessitate modified or different test methods than those used to date. Tests should be designed to more precisely relate corrosion events with specific microstructural features. For example, electrochemical corrosion methods could be used to oxidize the MWF beyond the corrosion potential so that the microstructural features of corrosion can be correlated more closely to known corrosion events. The passivation and breakdown of MWF materials could be induced using electrochemical methods and samples could be generated to study various stages of passivation, break down, and repassivation using TEM analyses to aid in interpreting corrosion in terms of the MWF microstructure. Of course, the layers formed by electrochemical methods must be shown to be equivalent to those formed

by corrosion in water or humid air. In conclusion, the following recommendations are provided as a means to increase knowledge of MWF corrosion:

- Perform TEM analysis on areas that have been characterized prior to corrosion. This will require the SEM to locate specific regions. An SEM “finders grid” embedded onto the MWF surface, or some other device, will be necessary to track these areas during TEM sample preparation. The most successful method to date is ultramicrotomy of the surface and underlying base metal.
- Design tests aimed at relating microstructure to specific corrosion events such as passivation, breakdown, repassivation, and pitting. For example, apply electrochemical corrosion tests to control the corrosion of MWF coupons for TEM analysis at various stages of passivation and breakdown.
- Study the contribution of localized corrosion events to U release.

These recommendations will probably require an initial phase of sample preparation development, and possibly the necessity to design new test methods, but will ultimately provide valuable input into unraveling the mechanism of MWF corrosion.

ACKNOWLEDGEMENTS

The TEM analyses documented in this report were conducted at ANL-Idaho, which is now part of the Idaho National Laboratory. The author would like to thank the following people for their contributions: Terry C. Totemeier for managerial support; Stephen G. Johnson for test solution data; Daniel P. Abraham, Dennis D. Keiser Jr, and William L. Ebert for valuable technical discussions and peer review of this document; and Shari K. Zussman for editorial assessment. This work was supported by the U.S. Department of Energy Office of Nuclear Energy, Science and Technology.

This report has been created by the University of Chicago as Operator of Argonne National Laboratory (“Argonne”) under Contract No. W-31-109-ENG-38 with the U.S. Department of Energy. The U.S. Government retains for itself, and others acting on its behalf, a paid-up, nonexclusive irrevocable worldwide license in said article to reproduce, prepare derivative works, distribute copies to the public, and perform publicly and display publicly, by or on behalf of the Government.

REFERENCES

1. J.E. Battles, J.J. Laidler, C.C. McPheeters, and W.E. Miller, "Pyrometallurgical Processes for Recovery of Actinide Elements," in *Actinide Processing: Methods and Materials*, eds. B. Mishra and W.A. Averill (The Minerals, Metals, and Materials Society, 1994), 135.
2. C. Pereira, M.C. Hash, M.A. Lewis, and M.K. Richmann, Ceramic Composite Waste Forms from Electrometallurgical Treatment of Spent Nuclear Fuel, *Journal of The Minerals, Metals & Materials Society*, **49** (1997), 24.
3. D.D. Keiser Jr. and S.M. McDeavitt, "Actinide-Containing Metal Disposition Alloys, in DOE Spent Nuclear Fuel & Fissile Materials Management," (American Nuclear Society, LaGrange Park, IL, 1996) p.178.
4. S.M. McDeavitt, D.P. Abraham, J.Y. Park and D.D. Keiser, "Stainless Steel-Zirconium Waste Forms from the Treatment of Spent Nuclear Fuel," *Journal of the Minerals, Metals & Materials Society*, **49** (1997), 29-32.
5. S.M. McDeavitt, D.P. Abraham, and J.Y. Parks, "Evaluation of Stainless Steel-Zirconium Alloys as High-Level Nuclear Waste Forms," *Journal of Nuclear Materials* **257** (1998), 21-34.
6. D.D. Macdonald, "Passivity-the key to our metals-based civilization," *Journal of Pure Applied Chemistry*, Vol. 71, No.6, (1999) 951-978.
7. A.T. Fromhold Jr. and S.J. Hoh, "The Transport of Ions and Electrons Through Microscopically Inhomogeneous Passive Films: Breakdown Implications," *Corrosion Science*, Vol. 29, No. 2/3, (1989), 237-255.
8. D.P. Abraham, J.W. Richardson Jr., and S.M. McDeavitt, *Mat. Sci. Eng.* A239-240 (1997), p.658.
9. D.D. Keiser Jr., D.P. Abraham, W. Sinkler, J.W. Richardson Jr., S.M. McDeavitt, "Actinide Distribution in a Stainless Steel-15 wt% Zirconium High-Level Nuclear Waste Form," *Journal of Nuclear Materials*, **279** (2000) 234-244.
10. D.D. Keiser, Jr., W. Sinkler, D.P. Abraham, J.W. Richardson, Jr., S.M. McDeavitt, "The Effect of Actinides on the Microstructural Development in a Metallic High-Level Nuclear Waste Form." *Rare Earths and Actinides: Science, Technology and Applications IV*. Bautista, R.G. and Mishra, B. eds. pp. 111-121 (2000).
11. J.S. Luo and D.P. Abraham, "TEM Characterization of Corrosion Products Formed on a Stainless Steel-Zirconium Alloy," *Scientific Basis of Nuclear Waste Management XXIII*, Material Research Society Symposium Proceedings, **608** (2000) 583-588.

12. B. Cox, H.I. Sheikeh, "Redistribution of the alloying elements during Zircaloy-2 Oxidation," *Journal of Nuclear Materials*, **249** (1997) 17-32.
13. B. Stellway, "The Mechanism of Oxide Film Formation on Austenitic Stainless Steels in High Temperature Water," *Corrosion Science*, **40**, No.2/3 (1998) 337-370.
14. J. Ensling, J. Fleisch, R. Grimm, J. Gruber and P. Gutlich, "A Corrosion Study of Austenitic and Martensitic Steels under Boiler Conditions by Means of ^{57}Fe Conversion Electron Mossbauer Spectroscopy," *Corrosion Science*, **18** (1978) 797-808.
15. B. MacDougall and M.J. Graham, *Growth and Stability of Passive Films: Corrosion Mechanisms in Theory and Practice*, ed. P. Marcus, J. Oudar; Marcel Dekker, Inc., 1995.
16. M.P. Ryan, M.F. Toney, A.J. Davenport, and L.J. Oblonsky, *In Situ X-Ray Diffraction Studies of Passive Oxide Films*, *MRS Bulletin*, July 1999.
17. D.P. Abraham, "Auger Electron Spectroscopy Study of MWF Alloys" ANL-CMTI-12365 (Sept. 99).
18. R.F. Voitovich, et.al., "Oxidation of Zirconium-Iron Alloys," translated from *Zashchita Metallow*, 17, No. 1, Jan-Feb (1981).
19. Johnson, S.G., et. al., *Radioactive Waste Management and Environmental Research*, 22 (2002), 300-326.

Distribution for ANL/05-09

Internal (Printed and Electronic Copies):

W. L. Ebert (10)

N.L. Dietz (10)

Internal (Printed Copy Only):

M. J. Steindler

Internal (Electronic Copy Only):

M. R. Hale, TIS

D. P. Abraham

C. H. Adams

R. K. Ahluwalia

T. H. Bauer

A. R. Brunsvold

D. B. Chamberlain

Y. I. Chang

J. C. Cunnane

T. H. Fanning

R. J. Finch

A. A. Foley

J. A. Fortner

E. K. Fujita

C. Grandy

D. J. Graziano

R. N. Hill

J. L. Jerden, Jr.

H. S. Khalil

J. J. Laidler

L. Leibowitz

R. M. Lell

D. Lewis

M. A. Lewis

C. J. Mertz

E. E. Morris

M. T. Peters

M. C. Regalbuto

C. T. Snyder

V. S. Sullivan

Y. Tsai

G. F. Vandegrift

R. A. Wigeland

M. A. Williamson

J. L. Willit

External (Printed and Electronic Copies):

R. W. Benedict, Idaho National Laboratory, Idaho Falls, ID (10)
K. M. Goff, Idaho National Laboratory, Idaho Falls, ID
D. E. Janney, Idaho National Laboratory, Idaho Falls, ID
D. D. Keiser, Jr., Idaho National Laboratory, Idaho Falls, ID

External (Electronic Copies Only):

M. A. Buckley, ANL Library-E

S. E. Aumeier, Idaho National Laboratory, Idaho Falls, ID
K. J. Bateman, Idaho National Laboratory, Idaho Falls, ID
T. J. Battisti, Idaho National Laboratory, Idaho Falls, ID
S. S. Cunningham, Idaho National Laboratory, Idaho Falls, ID
D. B. Davies, Idaho National Laboratory, Idaho Falls, ID
H. E. Garcia, Idaho National Laboratory, Idaho Falls, ID
S. G. Johnson, Idaho National Laboratory, Idaho Falls, ID
M. G. Gougar, Idaho National Laboratory, Idaho Falls, ID
D. D. Hagan, Idaho National Laboratory, Idaho Falls, ID
K. L. Howden, Idaho National Laboratory, Idaho Falls, ID
J. R. Kennedy, Idaho National Laboratory, Idaho Falls, ID
C. J. Knight, Idaho National Laboratory, Idaho Falls, ID
J. R. Krsul, Idaho National Laboratory, Idaho Falls, ID
C. E. Lahm, Idaho National Laboratory, Idaho Falls, ID
G. L. Lentz, Idaho National Laboratory, Idaho Falls, ID
S. X. Li, Idaho National Laboratory, Idaho Falls, ID
R. P. Lind, Idaho National Laboratory, Idaho Falls, ID
K. C. Marsden, Idaho National Laboratory, Idaho Falls, ID
S. D. McBride, Idaho National Laboratory, Idaho Falls, ID
H. F. McFarlane, Idaho National Laboratory, Idaho Falls, ID
T. P. O'Holleran, Idaho National Laboratory, Idaho Falls, ID
R. L. Parks, Idaho National Laboratory, Idaho Falls, ID
R. D. Phipps, Idaho National Laboratory, Idaho Falls, ID
C. L. Pope, Idaho National Laboratory, Idaho Falls, ID
S. R. Sherman, Idaho National Laboratory, Idaho Falls, ID
G. M. Teske, Idaho National Laboratory, Idaho Falls, ID
D. E. Vaden, Idaho National Laboratory, Idaho Falls, ID
D. L. Wahlquist, Idaho National Laboratory, Idaho Falls, ID
B. R. Westphal, Idaho National Laboratory, Idaho Falls, ID